Extensive Validation of the Three-Branch Model in Simulating the Static and the Dynamic Behavior of EDLC Supercapacitors

energies

MDPI

Article

Extensive Validation of the Three-Branch Model in Simulating the Static and the Dynamic Behavior of EDLC Supercapacitors

Mauro Zucca [1,*], Melika Hassanzadeh [1], Ornella Conti [1,2], Valter Giusio [1] and Umberto Pogliano [1]

[1] Istituto Nazionale di Ricerca Metrologica—INRiM, Strada delle Cacce 91, 10135 Torino, Italy; m.hassanzadeh@inrim.it (M.H.); ornella.conti@polito.it (O.C.); v.giusio@inrim.it (V.G.); u.pogliano@inrim.it (U.P.)
[2] Dipartimento Energia, Politecnico di Torino, Corso Duca degli Abruzzi 24, 10129 Torino, Italy
* Correspondence: m.zucca@inrim.it

Abstract

This study demonstrates the response of the three-branch equivalent circuit model in reproducing the terminal voltage of a supercapacitor that undergoes dynamic galvanostatic pulse trains for frequencies from 0.1 Hz to 100 Hz and signal amplitudes of 1 A, significantly wider than the sinusoidal signals used in impedance spectroscopy. Clean and accurate pulse trains were generated at different frequencies using a transconductance power amplifier, and the voltages at the supercapacitor terminals of three different sizes of supercapacitors were successfully compared with the model. The latter was also utilized to check its ability to accurately reproduce charging and self-discharging processes and the ability to simulate voltammetric cycles. This was verified for six supercapacitor sizes from 1 F (rated 1 mWh, 10 W) up to a large 130 F module (rated 70 Wh, 144 kW). In all cases, the relative difference, with respect to the rated voltage, between the terminal voltage provided by the measurements and that yielded by the model simulations did not exceed 3.5%. This extensive multi-level validation demonstrates how the identified three-branch model based on state equations can provide an accurate electrical design tool and a reference for standards.

Keywords: energy storage; electric double-layer capacitors; measurement; measurement accuracy; circuital modeling; supercapacitors

1. Introduction

Electric double-layer capacitors (EDLCs) have emerged as important components in modern energy storage designs because they offer high power density, remarkably fast charging, very high power, countless cycles of unchanged efficiency and long life. These characteristics make supercapacitors (SCs) suitable for energy storage in both static and dynamic environments, and many applications have been proposed in the technical literature [1,2] and implemented in situations characterized by pulsed loads, such as uninterruptible power supplies (UPSs), high-frequency switching, regenerative braking in automotives [3], aerospace applications [4], laser and military applications [2], and hybrid energy storage systems (HESSs) using batteries and SCs in parallel [5–7]. Progress has been made towards new supercapacitive materials [8], and new applications emerge every year, including the use of SCs in hybrid storage systems for grid forming, where the speed of intervention is crucial [9–11].

The ability to accurately and reliably model SCs and, in particular, the analysis of their dynamic response is important for the most recent and promising applications. For

Academic Editor: Jae-Hun Kim

Received: 28 January 2026
Revised: 21 February 2026
Accepted: 26 February 2026
Published: 28 February 2026

power applications, circuit models are well-suited for modeling because they can be easily integrated into the electrical models of the systems, including power converters and power grid models. The Scopus database has nearly 10,000 papers on SCs published in 2025 alone (9786 were recorded), which were found using the keywords "supercapacitor" or "EDLC". Many of these also deal with modeling. Therefore, it is difficult to comprehensively summarize the state of the art that has emerged in recent years in this field. Among the most popular equivalent circuit models (ECMs) in the literature, three models can be mentioned: the two-branch model, the three-branch model [12–20] and the fractional order (FO) models or fractional-order equivalent circuits (FOECs) [21–26]. The first two are commonly identified via galvanostatic charge–discharge (GCD) or galvanostatic charge–self-discharge (GCSD) measurements in the time domain, while the latter are identified via electrical impedance spectroscopy (EIS) analysis in the frequency domain. Studies in the literature generally focus on model validation, almost never deal with evaluating the model's ability to represent cyclic voltammetry (CV) and they rarely assess the model's ability to reproduce the dynamic response in the time domain, a feature rarely found in the literature beyond EIS. The dynamic response presented in the literature in terms of EIS is restricted to Nyquist or Bode diagrams. The EIS is limited to applying small sinusoidal current (galvanostatic EIS) or voltage (potentiostatic EIS) perturbations but does not provide the time response of the device to fast and consistent pulses and, above all, does not allow us to easily reconstruct the actual response waveform of the device and/or the model. The time response of an SC in terms of current and voltage waveforms is normally missed. Our consideration is not intended as a criticism of EIS but rather intended to emphasize that the time response to a pulse train provides different information from that provided by an EIS analysis. Indeed, EIS is based on the response to small sinusoidal signals and, therefore, relies on a single-harmonic signal of limited amplitude. A large pulse train imposes the response to a large signal with strong multi-frequency harmonic content.

This paper aimed to extensively validate the time-domain three-branch model [27] described on the basis of the circuit state equations identified with a nonlinear optimization [28,29], where the causes of uncertainty in the determination of the parameters have been carefully examined [30]. This study was developed at constant temperature using commercial SCs over several capacitance values, focusing on the model's ability to also reproduce voltammetric cycles. In this study, we utilized a special test system based on a transconductance amplifier, which can provide a very clean and accurate current pulse train to an SC in order to measure the voltage at the terminals and validate the model under dynamic conditions, with the train of pulses having a period from 10 ms to 10 s.

The novelty of this study, in addition to measuring and simulating the dynamic response of some commercial devices, is the extensive validation of the model in a broader sense. Indeed, in this study, we performed a wide model validation from capacitances ranging from 1 F to 400 F, including a big module of 130 F. The rated charging currents ranged from 800 mA to 80 A (peak 440 A), and the charging voltages ranged from 2.7 V to 62 V.

Finally, the measurements developed for this study consist of twenty datasets that are available on the public database Zenodo for the scientific community and also for the validation of models other than the one extensively validated by this study.

In summary, this study aimed to contribute to the effective use of SCs in dynamic environments to optimize their implementation in real-world applications.

2. Modeling Approach

2.1. Modeling: A General Panorama

A model for static applications can be easily built, where an SC is represented as a simple Thevenin equivalent circuit built by a capacitor having capacitance C in series with a resistor having resistance R_s: the equivalent series resistance (ESR). A parallel leakage resistor with resistance R_p can be introduced in parallel to C accounting for the discharge of the SC during the time when it is not supplied.

This simple model for capacitors was proposed as early as the second half of the 19th century and is generally attributed to Hermann von Helmholtz (see [31]). It remains the basis for the standards on SCs [32,33], which define the parameters that should be provided as SC specifications and usually suggest methods and procedures for determining such parameters. In this model, the SC behaves like a standard dielectric capacitor in series with a resistor constant, independent of frequency and voltage; it predicts a linear voltage rise when it is charged by a constant current and an immediate voltage drop when the supply current stops. Possible applications are the preliminary sizing of capacitor banks and calculation of their energy efficiency, where dynamic accuracy is not critical.

In order to account for the non-ideal behavior of SCs and because activated carbon with complex pore structures is used to maximize their surface area, the transmission line model (TLM) was proposed [34] and then developed by other authors [35], derived in principle from a physical model of a single porous electrode, even though ions must traverse a large number of convoluted paths in parallel to realize the full capacitance. The structure of the TLM is a ladder network of resistors and capacitors as shown in Figure 1a, which explains the reduction in the capacitance at increasing frequencies because ions only penetrate the mouth of the pores, so the effective resistance is low, and the accessible area of the electrode is small; by contrast, at low frequency, ions have time to diffuse to the bottom of the pores, increasing the effective capacitance to its nominal value, and the effective resistance also changes. Possible applications of the TLM are the electrochemical analysis of electrode materials and the detailed simulation of high-frequency switching noise in power converters.

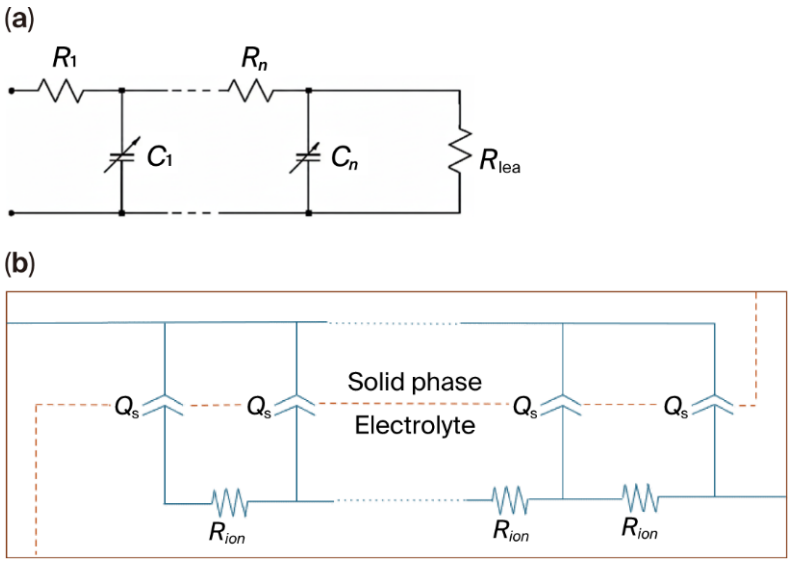

Figure 1. (**a**) TLM circuital model; (**b**) simplified form of the transmission line model for porous electrodes [36].

In recent years, fractional calculus has been applied for SC modeling, where, instead of using ideal capacitors, constant phase elements (CPE) are employed. In a CPE, the complex impedance is given as follows:

$$Z_{CPE} = \frac{1}{Q(i2\pi f)^{\gamma}} \quad (1)$$

where f is the frequency, Q is related to the electrode capacitance, and γ is the constant phase exponent. When γ is unitary, the impedance corresponds to an ideal capacitor.

The models obtained by the application of fractional derivatives seem to better fit some features of the Nyquist plots obtained with EIS measurement data, which often show semicircles or non-vertical tails not explained by ideal RC models, resulting in improved models for porous electrodes (Figure 1b). However, the dynamic temporal responses of fractional models are not easy to reconstruct [37]. A bridge between the simplicity of the RC models and the complexity of the TLM is the multi-branch modeling approach with different versions and number of branches; such models are the industry standards for dynamic power simulation. They are behavioral models that approximate the distributed nature of the pores using a finite number of RC branches with different time constants [15].

One particularly studied model is the three-branch model [38,39] organized as a first branch that explains the fast response (a time constant of the order of seconds); a second branch that simulates the delayed response due to the diffusion of the ions in the intermediate pores (time constant of the order of minutes); and, eventually, a third branch for the long-term settling of the ions in the deep pores (order of hours). The two-branch model is also widely used when long standby phases are of lower interest. The capacitance in the first branch can be modeled as a variable capacitance to account for the voltage-dependent width of the Helmholtz layer, and a high resistance can be connected in parallel to simulate the discharge of the supercapacitor over time. This model reproduces the charge redistribution phenomenon, where the voltage may increase after a discharge pulse stops, which is caused by charge slowly flowing back from the deep branches.

Table 1 summarizes a sample of recent and significant papers on supercapacitor circuit modeling using the most popular circuit modeling techniques, including two-branch and three-branch models and fractional order models. As can be seen, the identification approaches are diverse, and all the papers provide good or excellent results in the identification. Almost all the papers model one or a few SC samples, and only one of the papers attempts to model cyclic voltammetry, focusing mainly on that. The table shows that no paper analyzes the proposed model over short transients, and if they do, they do it mainly in the frequency domain.

Table 1. Sample of recent and significant papers on the supercapacitor circuit modeling.

Paper	Approach	Identification	Validation Scale	Time Domain Fast Pulse Trains
[13]	Two-branch circuital model	Zubieta optimized (MATLAB).	Slow cycles, seconds or more	--
[14]	Series model, Rs-C-Rp model, two branch model	Subspace system identification algorithms incorporating coulombic efficiency at 3 temperatures.	Pulse train frequency ~ 1 Hz	Electric motorcycle absorption trend
[15]	Three-branch model with additional resistive/capacitive elements on the first branch	Model parameters identified by means of the measurement data fitting. Energy efficiency, coulombic efficiency and differential capacitance tested. Test currents up to 130 A.	Charge–self discharge cycles. Great accuracy also in voltage drop simulation	--

Table 1. *Cont.*

Paper	Approach	Identification	Validation Scale	Time Domain Fast Pulse Trains
[16]	Three-branch model	Analytical identification, followed by a recursive least squares optimization. The model of a single SC is extended to SC banks. Discussion on residual charge phenomenon.	Accurate charge–self discharge validation. Pulse train periods of s or tens of s	--
[17]	One and two-branch models	The parameters have been calculated by analyzing the transient and the steady responses.	Charge–self discharge cycles	--
[18]	Three-branch model	The estimation procedure consists of two steps that combine an initial model parameter fitting (based on Zubieta) and a second step for fine-tuning the parameter values using the MATLAB Parameter Estimator module.	Validation on GCD cycles or charge–self discharge cycles with period of hundreds of seconds	--
[19]	Three-branch model	Model parameters obtained by an optimization approach combining the Osprey Optimization Algorithm (OOA) and the Parrot Optimizer (PO). This hybridization resulted in enhanced optimization performance.	The paper shows quasi-stationary voltage and current behaviors and no temporal transient data	--
[20]	Comparison of 5 models: one-, two- and three-branch (3b) and two 3b modified including [15]	The parameters of the 5 models are obtained by fitting the model generated output voltage onto the experimental voltage by means of the nonlinear least square solver (lsqnonlin) in MATLAB. Provided guideline for real-time simulation.	Charge–self discharge cycles. Harmonic excitation up to 50 Hz only in frequency domain	--
[21]	Fractional-order equivalent circuit (FOEC)	The method relies on a convolution, and by incorporating one degree of differentiation, the convolution is truncated to a finite series. FO estimation uses regularized least squares estimation to address the error drift.	Repetitive sawtooth current injected into the SC with rising time of 5 s or higher	--
[22]	FOEC (same as [21]) including leakage current. Included a FO extended Kalman filter	Model parameters experimentally identified. A state initialization method addresses the convergence issue of the estimator. Performance compared with the integer-order approach.	Current pulse 28 mA for 42 s, followed by a rest for an hour. Discharging current pulse lasts 14 s	--
[23]	Comparison of 4 FOEC plus RC. FO classic, FO RRCW, FO dynamic, FO transmission line	Model parameters optimized to achieve their best-fitting accuracy by using a genetic algorithm. Two indices are considered to evaluate the 5 model performances based on different test cycles.	Sawtooth current transients lasting seconds or tens of seconds	--
[24]	FO resonant model: (RC + fractional order parallel RLC)	The model parameters are obtained through the analysis of the experimental galvanostatic charge and discharge curve and the application of a heuristic optimization algorithm.	Validation on charge and discharge cycles with period > 1000 s	--

Table 1. *Cont.*

Paper	Approach	Identification	Validation Scale	Time Domain Fast Pulse Trains
[25]	Simplified Randles circuit model under CV and GCD investigations	Randles circuit parameters were extracted by fitting the cyclic voltammetry and galvanostatic charge–discharge (GCD) experimental data.	Validation on GCD cycles with period of s or tens of seconds e voltammetry cycles	--
[26]	FO R-L-C model with Warburg elements in parallel to C and L	Parameter dentification is obtained through measured Bode/Nyquist diagrams interpolation (C at low frequency impedance (Z), L high freq. Z. R mid-freq. range Z). 5th order polynomial expansion approximates the Warburg impedance.	Up to 300 kHz in the frequency domain. No experimental verifications in the time domain	--

The main novelty of this study compared to the literature studies is to provide an extended validation of the three-branch model, identified on the basis of the state-equations, on several SCs of very different sizes, rated voltages and currents; to extend the validation to cyclic voltammetry; and to provide the temporal response of the model to pulse trains having a frequency up to 100 Hz. Also, not to be overlooked is the fact that an original measurement circuit for the identification of the impulse response of the SCs is provided and that the measurement datasets are released to open access.

2.2. The Three-Branch Model to Be Extensively Validated

The model to be validated is shown in Figure 2. The parameters to be identified are the two capacitances of the first branch, the constant one C_{i0} and the voltage-dependent one C_{i1}, and the capacitances of the other two branches, C_d and C_l. The resistances R_d and R_l also need to be identified. The *ESR* R_i can be obtained from the measurements and kept as a known term in the model or included in the unknowns to be identified to reduce the discrepancy between the model predictions and measurements. Similarly, the leakage resistance R_{lea} can be measured and entered into the model as a constant or left as an unknown. In the modeling in this study, we included the measured *ESR* R_i, which was modified in a few cases by the identification process, while the initial R_{lea} was left as an unknown and always identified through the model identification procedure.

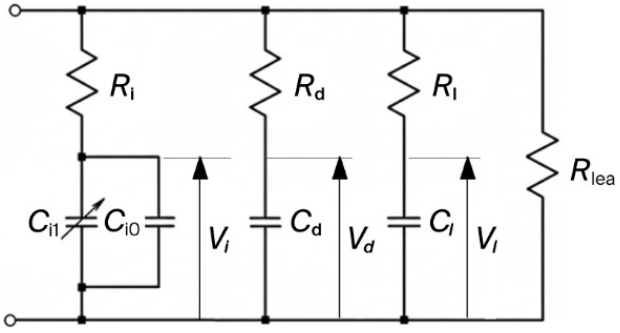

Figure 2. Three-branch electrical circuit model of an SC.

The leakage resistance is a nonlinear parameter that evolves over time, and in the case of intermittent sources with long stand-by phases, it should be identified with a specific measurement procedure as described in [29]. In this study, paying particular attention to impulsive behavior, the analysis was limited to fast transients from milliseconds up to a few tens of minutes and, in the latter case, only for identification measurements; therefore,

we only used the initial R_{lea} identified by the model, neglecting the nonlinear trend that emerged in the long stand-by phases lasting hours.

The identification process is described in detail in [29]; we report only the main steps below. The identification is based on the state equations of the circuit (2), where the state variables are the voltages across the capacitors (3). From the application of Kirchhoff's principles to the electric circuit, matrix $\boldsymbol{A}$ (5) and the constant term $\boldsymbol{B}$ (6) of the state Equation (2) are obtained. The unknown elements of the circuit are identified by minimizing the difference between the model results and the measurements in a nonlinear iterative process based on the conventional trust region reflection (CTRR) method [28]. The reference measurement is that of an SC charge, followed by a long self-discharge, because this measurement highlights all the circuit's time constants. The measured charging current behavior is used as the input for the model.

$$\dot{\boldsymbol{v}} = \boldsymbol{A}\boldsymbol{v} + \boldsymbol{B}y \tag{2}$$

$$\boldsymbol{v} = \begin{bmatrix} V_{\mathrm{i}} \\ V_{\mathrm{d}} \\ V_{\mathrm{l}} \end{bmatrix} \tag{3}$$

$$\dot{\boldsymbol{v}} = \begin{bmatrix} \frac{dV_{\mathrm{i}}}{dt} \\ \frac{dV_{\mathrm{d}}}{dt} \\ \frac{dV_{\mathrm{l}}}{dt} \end{bmatrix} \tag{4}$$

$$\boldsymbol{A} = \begin{bmatrix} \frac{-(R_{\mathrm{d}}+R_{\mathrm{l}})}{den\cdot C_{\mathrm{i}}(V_{\mathrm{i}})} & \frac{R_{\mathrm{l}}}{den\cdot C_{\mathrm{i}}(V_{\mathrm{i}})} & \frac{R_{\mathrm{d}}}{den\cdot C_{\mathrm{i}}(V_{\mathrm{i}})} \\ \frac{R_{\mathrm{l}}}{den\cdot C_{\mathrm{d}}} & \frac{-(R_{\mathrm{l}}+R_{\mathrm{i}})}{den\cdot C_{\mathrm{d}}} & \frac{R_{\mathrm{i}}}{den\cdot C_{\mathrm{d}}} \\ \frac{R_{\mathrm{d}}}{den\cdot C_{\mathrm{l}}} & \frac{R_{\mathrm{i}}}{den\cdot C_{\mathrm{l}}} & \frac{-(R_{\mathrm{i}}+R_{\mathrm{d}})}{den\cdot C_{\mathrm{l}}} \end{bmatrix} \tag{5}$$

$$\boldsymbol{B} = \begin{bmatrix} \frac{R_{\mathrm{d}}\cdot R_{\mathrm{l}}\cdot}{den\cdot C_{\mathrm{i}}(V_{\mathrm{i}})} \\ \frac{R_{\mathrm{l}}\cdot R_{\mathrm{i}}\cdot}{den\cdot C_{\mathrm{d}}} \\ \frac{R_{\mathrm{i}}\cdot R_{\mathrm{d}}\cdot}{den\cdot C_{l}} \end{bmatrix} \tag{6}$$

where

$$den = R_{\mathrm{i}}\cdot R_{\mathrm{l}} + R_{\mathrm{i}}\cdot R_{\mathrm{d}} + R_{\mathrm{d}}\cdot R_{\mathrm{l}} \tag{7}$$

and

$$y = i - i_{lea} \tag{8}$$

where i_{lea} is the leakage current.

The terminal voltage is obtained as

$$V_t = \frac{R_d\ R_l\ V_i + R_i\ R_l\ V_d + R_i\ R_d\ V_l + R_i\ R_d\ R_l\ (i - i_{lea})}{den} \tag{9}$$

CTRR optimization.

The CTRR algorithm addresses the optimization as a least square problem:

$$\min_x \|F(x)\|^2 = \min_x \sum_i F_i^2(x) \tag{10}$$

where F(x) can be a vectorial function or a scalar function f(x). A local quadratic approximation of f(x) around the current point x is built using the first two terms of the

Taylor approximation, q(s). This function correctly represents the behavior of f(x) in a 'neighborhood' of the current point x. The trust region subproblem can be finally defined as

$$\min_s \{q(s) \; subjected \; to \; \|s < \Delta\|\} \tag{11}$$

where Δ is the radius of the trust region.

$$f(x+s) \approx q(s) = f(x) + g^T s + \frac{1}{2} s^T H s \tag{12}$$

where g is the gradient of the function $f(x)$ evaluated in the current point and H is the Hessian of the function. The derivative of the function (11) (excluding the term $f(x)$ since it is not s-dependent) is evaluated and set equal to zero in order to find the minimum:

$$\min_s \left\{ g^T s + \frac{1}{2} s^T H s \right\} \tag{13}$$

if the condition

$$f(x+s) < f(x) \tag{14}$$

is satisfied, the point is updated from x to $x + s$.

In the case of this study, F(x) is a vector function for which the i-element is defined as the difference between the measured terminal voltage values and the ones obtained by the model.

$$r_i(x) = V_{tmeas_i} - V_{tmodel_i}(x) \tag{15}$$

$$F(x) = \begin{bmatrix} r_1(x) \\ r_2(x) \\ \vdots \\ r_i(x) \end{bmatrix} \tag{16}$$

The function F(x + s) is approximated with the first term of the Taylor approximation:

$$F(x+s) \approx F(x) + Js \tag{17}$$

where J is the Jacobian of $F(x)$ evaluated in the current point, x. The problem is defined as

$$\min \|F(x+s)\|^{\,2} \approx \min \|F(x) + Js\|^2 \tag{18}$$

It is possible to take into account $\|F(x) + Js\|^2 = (F(x) + Js)^T (F(x) + Js)$, consider the derivative and set that equal to zero to find the minimum, so that the solution for the problem is

$$J^T Js = -J^T F \tag{19}$$

At the end, if the condition

$$F(x+s) < F(x) \tag{20}$$

is satisfied, the point is updated from x to $x + s$.

Temperature constancy.

In this study, we needed a repeatable and stable model to validate it across different tests (GCD, GCSD, CV, dynamic) developed at different times but under the same laboratory conditions. Therefore, in our study, the temperature was kept constant at 23 °C ± 1 °C for each test in a climatic chamber because, otherwise, the identified model parameters would have been varied, jeopardizing the extensive validation.

3. Measurements: Samples, Systems and Methods

Five sizes of commercial SCs were analyzed in this study: 1 F, 10 F, 25 F, 60 F, and 400 F. For each size, we measured four identical SCs (three for the size 25 F). These SCs have nominal voltages between 2.7 V and 3 V and rated currents between 800 mA and 26 A. Additionally, we characterized a large 130 F module, with a nominal voltage of 62 V and a rated current of 80 A, which we also tested in the case of quick discharge at 440 A. The main parameters of the analyzed SCs are reported in Table 2.

Table 2. Manufacturer specifications of the considered single SCs and the module.

SC Size	Rated Voltage	Max *ESR* (mΩ)	Rated Current (A)	Stored Energy (Wh)	Peak Power (kW)	Pulse Current (A)
1 F	2.7	200	0.80	0.001	0.01	1.10
10 F	3.0	26.0	3.70	0.012	0.09	12.0
25 F	3.0	18.0	4.20	0.031	0.12	26.0
60 F	3.0	13.0	6.70	0.075	0.17	51.0
400 F	2.7	3.20	26.0	0.410	0.57	220
130 F *	62	6.70	80.0	69.60	144	2157

* Module.

Within the MetSuperCap project [40], all the performed measurements are reported in the Zenodo public database inside the project community. The measurements presented here are reported in detail in the following datasets:

- 1 F [41–44]; 10 F [45–48]; 25 F [49–51]; 60 F [52–55]; 400 F [56–59]; 130 F [60].

The MetSuperCap community database includes measurements from various commercial brands. The purpose of the datasets is to build a database for model development and scientific analysis, not to compare the performance of different commercial brands. This is because the SC's performance can vary depending on the storage conditions, terminal fixtures, and measurement methods; moreover, the specifications released by manufacturers have wide tolerances, whose orders of magnitude are tens of percents. The commercial brand of SCs, therefore, remains anonymous within the project and within this paper.

3.1. Measurement Systems

Two measurement systems were used for the charge–discharge and voltammetric analysis in this study:

- For SCs from 1 F up to 400 F, Biologic BCS 810 and BCS 815 (Biologic, Seyssinet-Pariset, France) two-quadrant generation and measurement modules, combined with a climatic chamber, were used (Figure 3). The Biologic modules allow for charge and discharge, charge and self-discharge and voltammetric cycle measurements. The combination with the climatic chamber allowed for all measurements to be carried out within a controlled temperature of 23 ± 1 ° C. The temperature of the SCs was controlled with a thermocouple, and in order to limit the temperature increase of the SCs during the tests, the charging and/or discharging electric current was kept lower than the rated current. The BCS 810 and BCS 815 systems were calibrated with the BCS-CAL system based on a calibrated reference multimeter.
- For the 130 F module, two Itech IT6015C 80 V, 15 kW two-quadrant DC power supplies were used (ITECH Power Supply, Nanjing, Jiangsu Province, China), connected in parallel. For the current measurement, a LEM IT 205-S Ultrastab transducer (80 A pk) and a LEM ITZ 2000-50-PR (440 A pk) were used (LEM International SA, Meyrin-

Geneva, Switzerland), while the voltage was measured with a Tunkia TH0150 voltage divider (TUNKIA Co., Ltd., Changsha, Hunan, China). The measurements were acquired with a two-channel PXI 4461 card that was calibrated at INRIM, with an acquisition software developed in LabView (Figure 4).

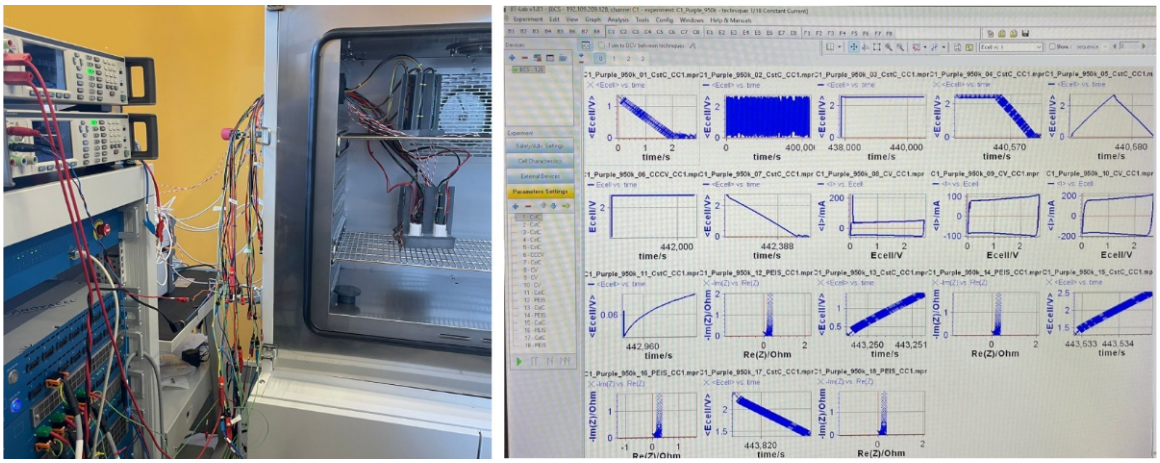

Figure 3. On the (**left**) is the preparation of the measurement setup with BCS 810 and BCS 815 galvanostats–potentiostats with SCs in the climatic chamber. On the (**right**) is a screenshot of the Biologic BT-Lab™ (version 3-0-1) measurement and acquisition software during tests. All measurement data are available open access in the datasets associated to this study).

Figure 4. The generation and measurement system for the 130 F module. The current transducer in the image is the LEM IT 205-S Ultrastab for the 80 A peak, which was replaced with a LEM ITZ 2000-50-PR transducer and related amplifier in the case of the 440 A peak.

Because the repeatability of the measurements is strongly influenced by the quality of the fixtures and by the mechanical stress on the electrodes, the cables were soldered onto the terminals of the SCs and fixed to a 3D-printed support in order to avoid mechanical stress (Figure 5). This was not necessary for the 130 F module, which has robust terminals tightened with bolts on a threaded stem. The current and voltage (sense) terminals were inserted using the 4-terminal insertion principle to avoid counting contact resistances when measuring the *ESR*.

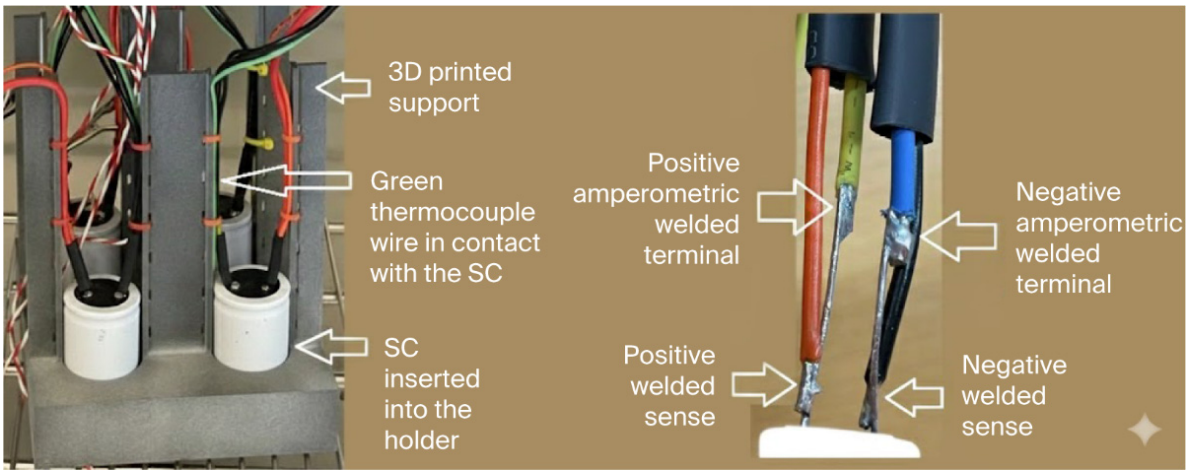

Figure 5. Details of the terminal connections and mounting on the printed support to avoid mechanical stress and to accommodate the thermocouples in contact with the SCs.

3.2. Measurement Method and Quantities

All the SCs underwent preconditioning, as defined in [30], which consisted of alternating 30 min charging cycles, followed by charging and self-discharging. These cycles were repeated 10 to 20 times. Preconditioning, or training, allows for good repeatability of the device and, therefore, of the measurements. For brevity, we will not report the preconditioning behaviors here, which are nevertheless available in the datasets, but we only report the final measurements on the trained SCs. The measurements consist of the following:

1. A constant-current charging cycle up to the nominal voltage, followed by a long self-discharge at zero current. From this cycle, the parameters of the three-branch equivalent circuit can be identified according to the methodology described in Section 2.2, and an initial *ESR* measurement was performed. The ESR_{ch_sd} was computed according to Formula (21) and Figure 6 as the ratio between the voltage drop ΔV_{ch-sd}, which appears when the charging current stops, and the charging current I_{ch}.

$$ESR_{ch\_sd} = \frac{\Delta V_{ch-sd}}{I_{ch}} \tag{21}$$

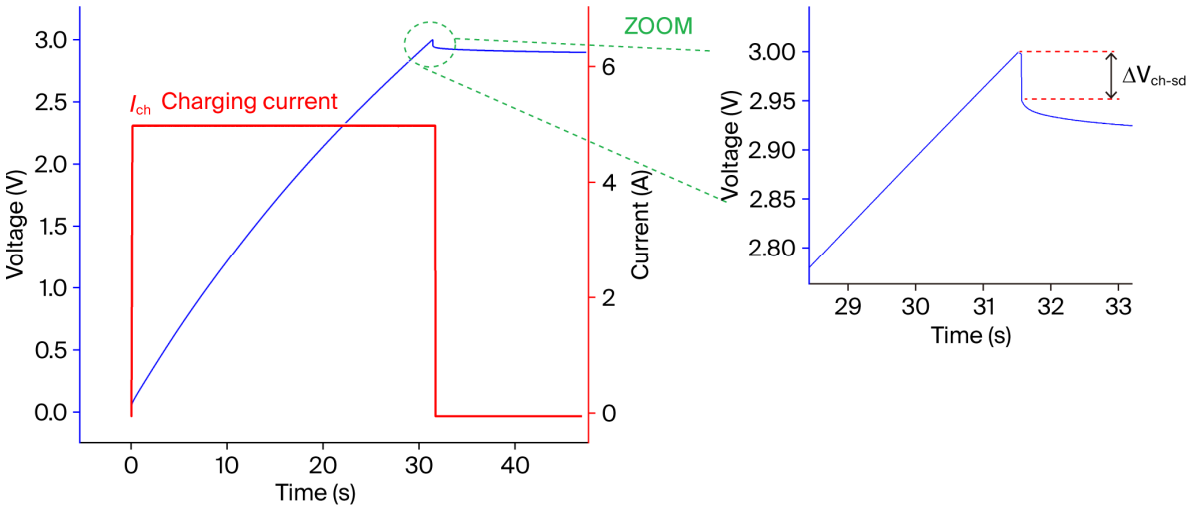

Figure 6. Charge and self-discharge (ch-sd) of a 60 F SC. *ESR* was calculated as the inverse ratio between the charging current I_{ch} and the voltage drop ΔV_{ch-sd}, which appears when the charging current stops.

The measured charge and self-discharge cycles are shown in Figure 7 for the considered SCs. Apart from the 130 F module, the curves for three/four identical SCs of the same size are shown for all the other sizes in Figure 7. As can be seen, the discrepancies are below 10 mV, except for 60 F, which is below 20 mV, and the relative differences related to the rated voltage are below 0.35% and 0.70% for 60 F. As highlighted in [30], the expanded uncertainty on the equivalent circuit model (ECM) parameter determination can be estimated on the order of 1%; therefore, we can state that the measurements on the analyzed samples of the same size suggest that a single circuit could be suitable for simulating all of them. In any case, in the following, the comparison between measured and simulated results will refer to the same sample on which the ECM is identified.

2. A cycle consisting of a constant-current (cc) charge up to the nominal voltage combined with 30 min of constant-voltage (cv) charging, followed by a complete constant-current discharge. We call this cycle cccv in the following. From this measurement, the stored energy in the SC is calculated, and the *ESR* is evaluated in the discharging phase. Such an *ESR* is used to evaluate the maximum power; moreover, this cycle is the one normally considered as a reference in the European standards [14,15]. The series resistance is computed as follows (Figure 8):

$$ESR_{cccv} = R_{en} = \frac{\Delta V_{cccv}}{I_{dis}} \tag{22}$$

where I_{dis} is the discharging current, usually equal to the charging current.

The capacitance is calculated during the discharging phase as follows:

$$C_{dis} = \frac{I_{dis} \cdot (t_2 - t_1)}{U_1 - U_2} = \frac{I_{dis} \cdot \Delta t}{\Delta U} \tag{23}$$

- U_1 is the measured start voltage at time t_1. It is equal to 80% of the SC rated voltage.
- U_2 is the measured end voltage at time t_2. It is equal to 40% of the SC rated voltage.
- t_1 is the time at which the terminal voltage of the SC reaches the value U_1 from the start of the discharge.
- t_2 is the time at which the terminal voltage of the SC reaches the value U_2 from the start of the discharge.

The capacitance can also be computed with the energy method as follows according to [32]:

$$C_{en} = \frac{2\,W}{{U_1}^2 - {U_2}^2} = \frac{2\int_{t_1}^{t_2} I_{dis}(t)U(t)dt}{{U_1}^2 - {U_2}^2} \tag{24}$$

The stored energy in the SC can be computed during the charging phases (both cc and cv) or during the discharging phase, as follows:

$$\Delta W = \int_{t_0}^{t_c} I_{ch}(t) \cdot U(t)\, dt + \int_{t_c}^{t_d} I_{cv}(t) \cdot U_R(t)\, dt \tag{25}$$

where t_0 and t_c are the starting charging time and the ending charging time at constant current cc, $I_{cv}(t)$ is the charging current at constant voltage cv, and t_d is the cv ending time, respectively. $U(t)$ is the voltage during cc charging, and $I_{cv}(t)$ is the current behavior during cv charging.

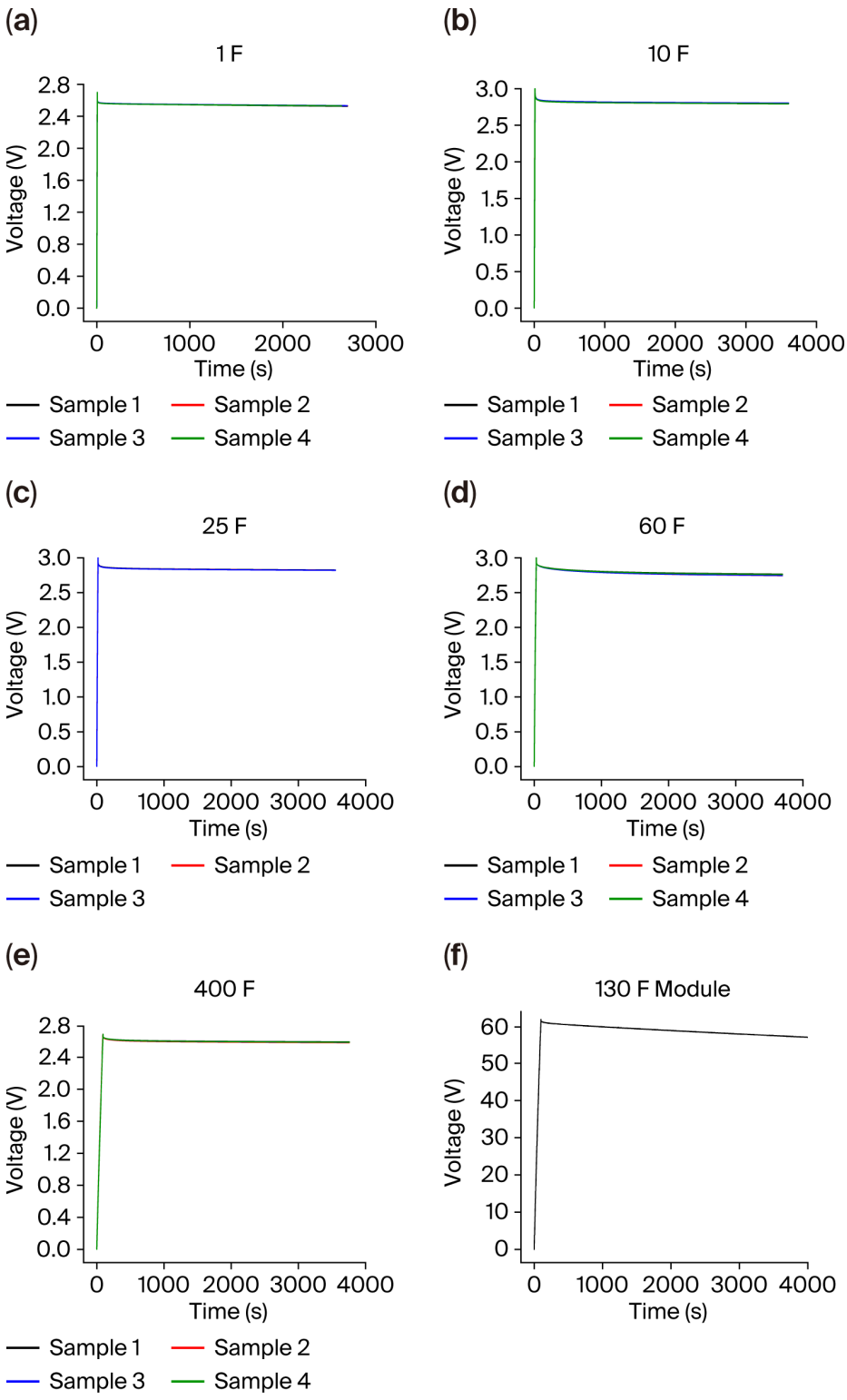

Figure 7. Charge and self-discharge process for different SC sizes: (**a**) 1 F; (**b**) 10 F; (**c**) 25 F; (**d**) 60 F; (**e**) 400 F; (**f**) 130 F. Diagrams show the behavior of the SC samples for each size during the charge and self-discharge process after preconditioning. For every family of SCs except 130 F, the diagrams show how the measured terminal voltage for each sample is very close to the other ones, with discrepancies below 10 mV, except for 60 F, which is below 20 mV, and relative differences related to the rated voltage are below 0.35% and 0.70% for 60 F. This means that samples of the same family have similar behaviors and very close circuit parameters. When not all colors are visible, it means the lines overlap.

Alternatively, we can have the following:

$$\Delta W = \int_{t_d}^{t_e} I_{dis}(t) \cdot U_d(t)\, dt \tag{26}$$

where t_d and t_e are the discharging start time and end time, respectively; U_d(t) is the voltage during discharging; and I_{dis} is the discharging current.

Finally, according to [32], we can define the maximum power as follows:

$$P_{max} = \frac{1}{4} \cdot \frac{{U_R}^2}{ESR_{cccv}} \tag{27}$$

where U_R is the rated voltage of the SC.

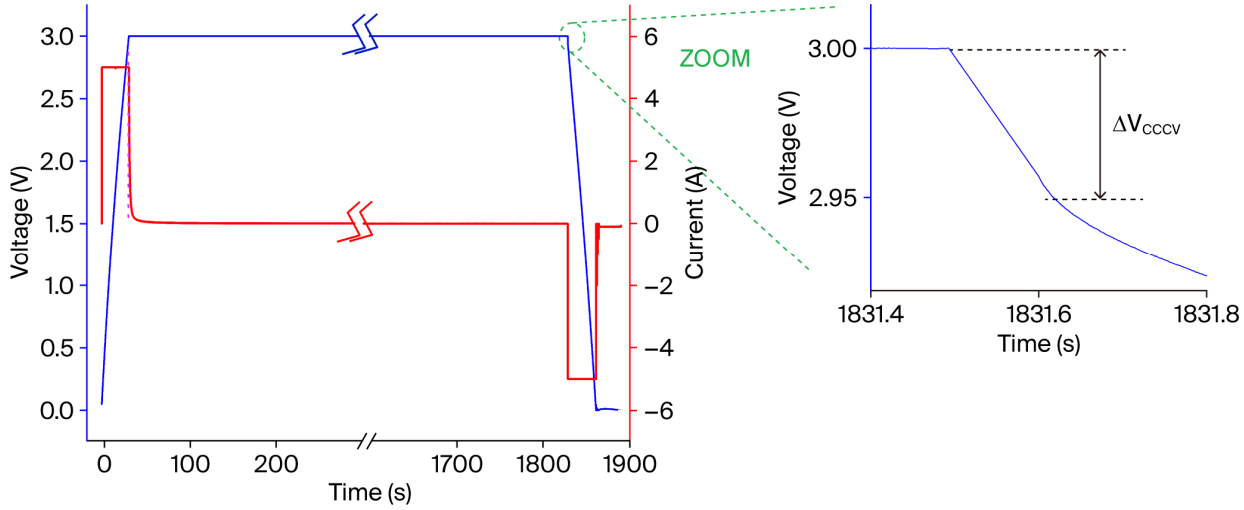

Figure 8. Constant current (cc), constant voltage (cv) and discharge cycle of a 60 F SC. ESR is computed during the discharge phase as the inverse ratio between the discharging current I_{dis} and the voltage drop ΔV_{cccv}, which appears when the discharging current starts. This cycle is a reference for standards [32,33]. In the figures the blue line refers to the terminal voltage at the and the red line refers to the current.

3. A charge cycle and immediate discharge. This allows for estimating the *ESR* in a different way.

The charge–discharge (ch-dis) is performed with the same current: $I = I_{ch} = -I_{dis}$.

When the rated voltage is reached, a voltage drop due to the *ESR* appears, and immediately, an additional voltage drop appears due to the discharging current (Figure 9). The series resistance can be evaluated as follows:

$$ESR_{ch_{dis}} = \frac{\Delta V_{ch-dis}}{2 \cdot I} \tag{28}$$

4. Cyclic voltammetry (uppercase CV to distinguish from constant voltage cv) is achieved by applying a linear variation in the voltage at the SC terminals from zero to the rated value and vice versa, according to a triangular waveform (Figure 10a). In this technique, the rate of voltage change over time, or the derivative of the voltage over time, is constant and is referred to as the scan rate.

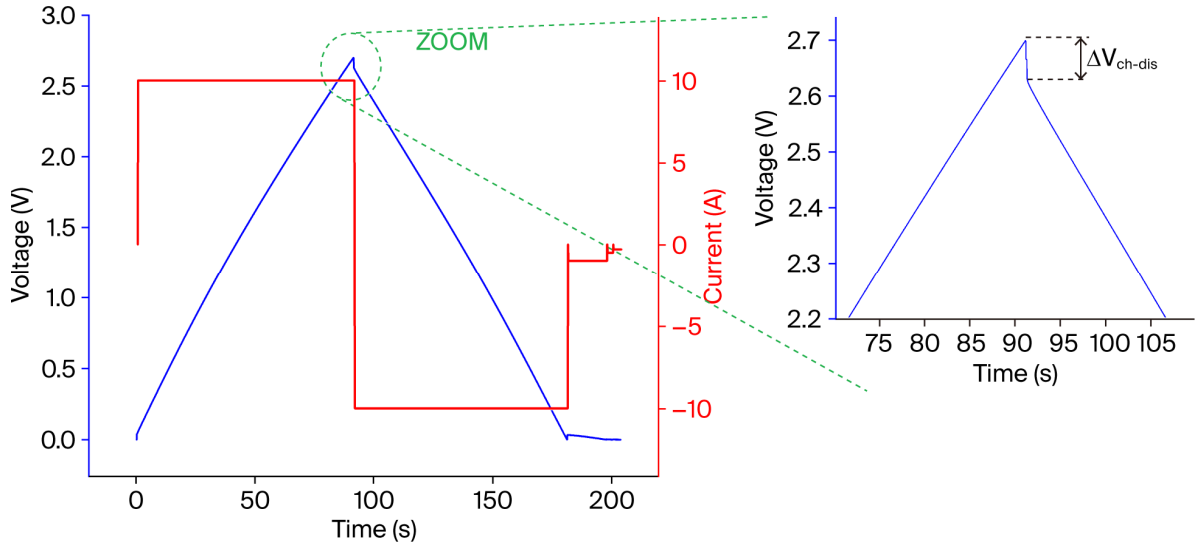

Figure 9. Charge at cc up to the rated voltage and immediate discharge at cc for a 400 F SC. Charge and discharge (ch-dis) are supplied with the same current. In the figures the blue line refers to the terminal voltage at the and the red line refers to the current.

$$s = \frac{dV}{dt} = constant \tag{29}$$

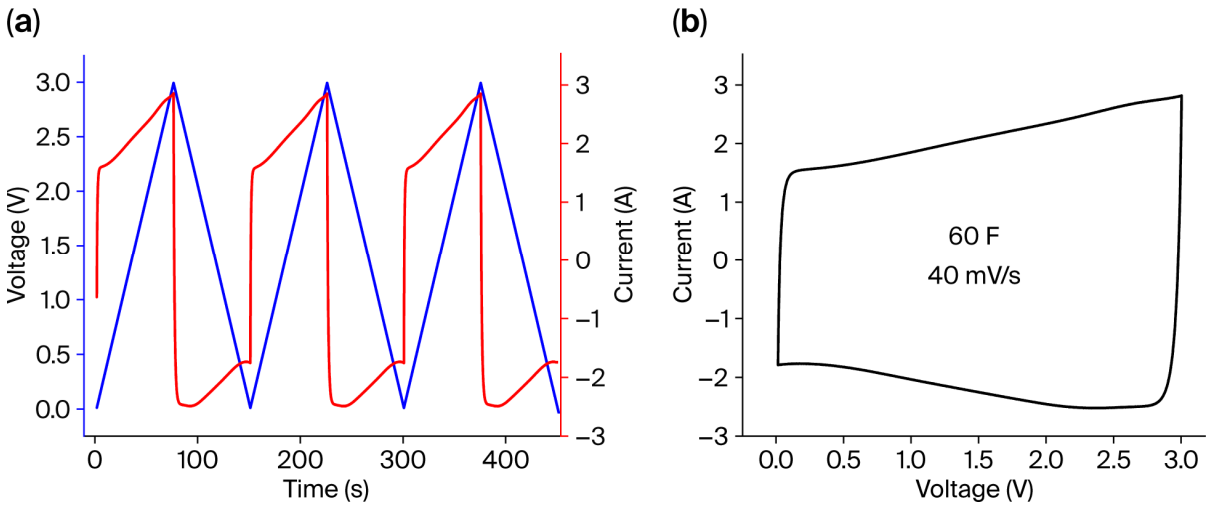

Figure 10. (**a**) Triangular imposed voltage–time behavior (in blue) and consequent current–time behavior (in red) during the cycling voltammetry test on a 60 F SC. (**b**) CV behavior in the current–voltage plane. After a couple of stabilization cycles, the behavior becomes repeatable. Here, only stabilized behavior is reported.

After a couple of settling cycles, the current–voltage diagram at the terminals produces repeatable cycles (Figure 10b) whose area is proportional to the SC capacitance. In particular, the capacitance is obtained as follows [61].

The capacitance is defined as the derivative of the stored charge Q with respect to the applied potential V:

$$C(V) = \frac{dQ}{dV} \tag{30}$$

During CV measurements, the applied potential varies linearly according to the constant scan rate s. Because the current is defined as $I = dQ/dt$, the differential charge can be expressed as follows:

$$dQ = I(V)\,\frac{dV}{s} \tag{31}$$

By integrating over the entire potential window ΔV, the integral between the zero and the rated voltage, the total charge transferred during a CV charging part is given by the following:

$$Q = \frac{1}{s}\int_{\Delta V} I(V)\,dV \tag{32}$$

The average capacitance C is obtained by normalizing the charge with respect to the applied potential window:

$$C = \frac{Q}{\Delta V} \tag{33}$$

Taking into account both the forward (charging) and reverse (discharging) scans of the CV cycle, the charge transmitted to and received from the SC is computed twice by integrating on the total area of the CV. Therefore, the capacitance is calculated as follows:

$$C = \frac{1}{2\,s\,\Delta V}\oint I(V)\,dV = \frac{Area}{2\,s\,\Delta V} \tag{34}$$

For commercial SCs, these cycles tend to underestimate the capacitance, which also depends on the rate of voltage change. In the author's experience, the capacitance increases upon decreasing the scan rate s.

CVs are not typically used in testing, but they are important in electrochemistry, where the CV curve symmetry and shape reveal information about the SC's electrochemical behavior, including the contributions of ion diffusion, faradaic reactions, and capacitive and pseudocapacitive processes.

4. Measurements and Simulation Results

The measurement results are analyzed in this section. After discussing some preliminary measurements, the charge and self-discharge measurements used to identify the three-branch model are presented, along with how the model reproduces them. The capacitance measurements obtained using the methods described in Section 3.2, Point 2, and the capacitance measurements obtained using cyclic voltammetry (Section 3.2, Point 3) are then analyzed, including how the model reproduces these results.

4.1. Preliminary Measurements

A series of preliminary measurements were performed on the SC samples considered to evaluate their behavior. The results are reported in Table 3 and analyzed according to the measurements and formulas described and reported in Section 3. All the measured quantities are better than the minimum specifications declared by the manufacturers; in particular, the measured *ESR* is always lower than that in the specifications, and the stored energy and the maximum power are always higher than those in the specifications even though, as highlighted in Section 4.3, the measured capacitance is sometimes lower.

The table provides interesting information about the series resistance. Its value varies significantly depending on the measurement method. Generally, the ch-dis and ch-sd methods provide values closer to each other than the cccv discharge method. However, the latter is the "cleanest" in the sense that the voltage drop is sharper. Taking the ch-dis method as a reference, the relative variations in *ESR* compared to the other two methods range from a few percent up to 19.6% in the case of 25 F samples and to 30.6% in the case of 1 F. This last case is peculiar, however, because the generator that is used only for 1 F

has a significant delay in the current reversal, and this leads to anomalous results. Even the variations in *ESR*, using the same method, between samples of the same size can reach almost 20% (19.2% in the case of 25 F samples). The sampling time of the measurements can influence these determinations, which, in the case of the measurements examined here, was 2 ms. Given this premise, a discussion of the accuracy of *ESR* measurements would require a broad and specific discussion, which is beyond the scope of this study.

Table 3. Measured and computed results concerning *ESR*, energy, power and efficiency.

SC Size	Sample Number	$ESR_{ch\text{-}dis}$ (mΩ)	$ESR_{ch\text{-}sd}$ (mΩ)	ESR_{cccv} (mΩ)	Stored Energy (mWh)	Max Power (W)	Efficiency
130 F * (I_{ch} = 80 A)	#1	5.08	4.50	4.50	$79.56 \cdot 10^3$	$192 \cdot 10^3$	0.99
130 F * (I_{ch} ~≅ 440 A)	#1	n.a. **	4.66	4.83	$79.55 \cdot 10^3$	$192 \cdot 10^3$	0.99
400 F	#1	3.00	2.93	2.68	398	680.5	0.97
	#2	3.32	3.12	2.67	419	681.5	0.97
	#3	2.90	2.90	2.65	403	688.4	0.97
	#4	3.05	2.70	2.67	419	681.5	0.98
60 F	#1	10.0	10.0	8.94	77	251.8	0.90
	#2	9.80	10.0	8.50	87	264.1	0.98
	#3	10.0	9.70	8.32	84	219.06	0.98
	#4	9.82	9.40	8.32	84	219.06	0.98
25 F	#1	17.7	16.6	14.8	37	152.3	0.97
	#2	17.4	16.6	14.5	35	155.3	0.97
	#3	14.3	17.1	15.5	36	145.30	0.97
10 F	#1	24.5	22.8	21.0	17	107.11	0.98
	#2	24.4	23.2	20.6	15	109.13	0.98
	#3	22.5	24.0	22.2	16	101.17	0.98
	#4	24.5	24.0	21.0	15	107.21	0.98
1 F	#1	170	118	162	0.91	11.21	0.94
	#2	160	114	155	0.96	11.75	0.94
	#3	167	120	156	0.96	11.65	0.94
	#4	160	114	158	0.95	11.54	0.94

* Single big module: mass ~16 kg, length ~70 cm including terminals. ** test not performed for thermal limitations.

Note that, in the identification procedure for the models, the measured ESR_{cccv} (R_{en} in the datasets) was taken as the value of the first attempt (starting value). This quantity was, however, included as an unknown in the optimization and identification process and was generally retained by the model identification and optimization process in the cases 1 F, 10 F, 25 F and 60 F. On the contrary, in two cases, the initial *ESR* was significantly modified to improve the fitting over a wide time span, namely in the 130 F and 400 F cases.

The SC samples that were analyzed for model identification are the only sample 130 F, sample #2 400 F, sample #3 60 F, sample #1 25 F, sample #1 10 F, and sample #1 1 F.

4.2. Three-Branch Model Identification and Results

The identification process described in Section 2.2 was applied to the six SC samples representing six different sizes. The process, based on the charge and self-discharge measurement, allows for the identification of the circuit parameters included in the equivalent ECM for the simulation of the same cycles used for identification. The simulations were performed with the LTSpice™ software (version 26.0.1), and the identified parameters used for the simulations are reported in Table 4.

Table 4. Parameters of the equivalent three-branch ECM of the different SC sizes. The circuit is reported in Figure 2. Comparison of charge and self-discharge cycles is reported in Figure 11.

Cap	R_i/mΩ	C_{i0}/F	C_{i1}/FV^{-1}	R_d/Ω	C_d/F	R_l/Ω	C_l/F	R_{lea} *	I_{ch}/A **
1 F	120.0	0.767	0.073	169.3	0.039	29931	0.023	2.0 MΩ	0.50
10 F	21.00	5.490	1.028	21.78	0.626	1538.5	0.128	40 kΩ	2.50
25 F	14.0	14.03	2.534	22.69	0.945	340.7	0.261	5.3 kΩ	3.50
60 F	8.50	33.05	6.682	14.66	2.182	204.4	2.488	3.2 kΩ	5.00
400 F	4.09	260.3	29.04	8.225	10.47	333.9	4.710	5.0 kΩ	10.0
130 F	12.78	103.5	0.374	117.6	1.274	1511.2	0.986	0.5 kΩ	80.0

* The leakage resistance was introduced as an unknown in the identification process, and the estimate includes the open circuit impedance of the generator used in the measurements. ** The last column shows the magnitude of the constant charging current.

Regarding the 130 F module, it is important to note that, in this study, the purpose of the identification performed is to consider the module as a whole, obtaining the behavior of an equivalent SC. Clearly, this approach differs from that of other studies, whose goal is to develop a model of the module based on the characterization of the individual cells. In our case, when the behavior is repeatable and we have verified that, the interaction between individual cells within the module can be ignored in the overall simulation.

The comparison results are shown in Figure 11 in six diagrams, one for each analyzed sample. The figures contain two graphs each: the comparison diagram and the relative percentage error graph, computed as the relative percentage difference between the measured and simulated terminal voltage, referred to as the rated voltage. As can be seen from the figures, the relative error in the regions of maximum discrepancy does not reach 60 mV (2%) for the 1 F, 25 F and 400 F samples, while it does not reach 75 mV (2.5%) for the 10 F and 60 F samples; in the other regions, it is much lower. In the case of the 130 F module, it does not exceed 1.5%.

It can be noted that the error distribution has a similar trend for all SCs. The identification process occurs by minimizing the model results with respect to the measurement of a charge and self-discharge cycle performed on the preconditioned SCs. The measurement of this cycle does not differ significantly as the capacitance increases, except for a variation in charging times on the order of seconds or tens of seconds. This does not substantially alter the identification process, which is influenced by other factors, such as temperature, measuring noise, or the parameters chosen for the convergence of the identification algorithm. In the case study with measurements in a controlled environment, the temperature is constant, the measurement noise is minimal and essentially constant, and the parameters for the optimization algorithm are verified by the good convergence of the algorithm itself. This explains why there are no substantial differences in the distribution of the relative error. Only in the 130 F module do we observe a reduction in the amplitude of the relative error, which may be due to the higher rated voltage compared to that of the other SCs.

In light of these results, it can be stated that the model is extensively validated under quasi-static conditions over a wide range of capacitances.

From the diagrams, it is worth noting that the self-discharge rate is rather limited except for the 130 F module. This is because, according to the manufacturer's specification, the SCs considered in this study generally have a leakage current on the order of 2.5 μA/F except the 130 F module, which has a leakage current that varies from 40 μA/F up to almost 1 mA/F depending on the type on the market, and we used a module of the second type. This explains the considerable self-discharge of the module.

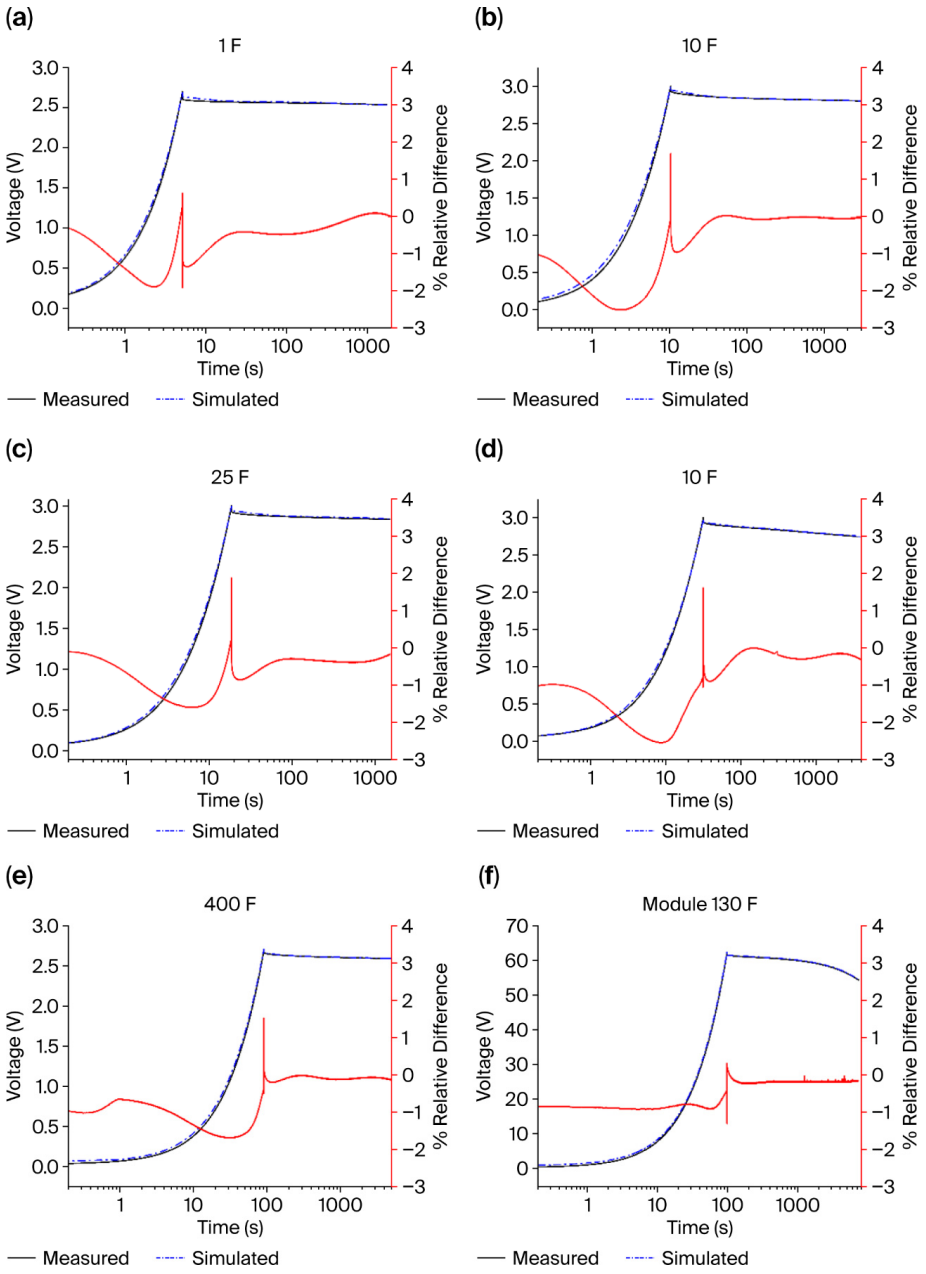

Figure 11. Three-branch ECM validation for the different SC sizes: (**a**) 1 F; (**b**) 10 F; (**c**) 25F; (**d**) 60 F; (**e**) 400 F; (**f**) 130 F. Diagrams show the computed (black lines) and simulated (dotted blue lines) behaviors, and on the right, the red scale represents the relative difference with respect to the rated voltage. This latter is high at the peak voltage but always below 2% and tends to zero (few mV) during self-discharge (static situation). A high-level relative discrepancy also appears during the first part of the charging but is always below 2%, being 60 mV for a 3 V rated voltage and 54 mV for a 2.7 V rated voltage. To make the relative discrepancy more evident, the semilogarithmic scale is introduced. Only in the case of 60 F and 10 F SCs does the maximum error reach 75 mV (2.5%).

4.3. Three-Branch Model Utilized to Simulate Voltammetry Cycles

For each SC sample, except for the 130 F module, three voltammetric cycles were measured at three different scan rates. All cycles are available in the dataset. For brevity, only the cycles at the two highest scan rates, which provide the largest area, are reported here. The capacitance values measured at the lowest scan rate, which provides the highest capacitance, are reported in Table 5. The table also reports the measured capacitances with the discharge method and the energy method, C_{dis} and C_{en} in accordance with (23) and

(24). Concerning the 130 F module, it was not possible to measure the voltammetric cycles up to the rated voltage of 62 V because the Biologic potentiometers are limited to 9 V. Using a Keithley 2461 Source Measure Unit (Keithley Instruments LLC, Solon, OH, USA), it was possible to measure a voltammetric cycle up to the voltage of 20 V, with the sole purpose of verifying the three-branch ECM.

Table 5. Capacitances measured with the discharge methods and the energy method, C_{dis} and C_{en} in accordance with (23) and (24). The last column reports the capacitance calculated from the area of the measured voltammetric cycles (34) with the minimum scan rate used in the measurements.

SC Size	Sample Number	C_{dis} (F)	C_{en} (F)	C_{CV} (F) *
130 F (80 A)	#1	133.4	134.0	Not available
130 F (440.5 A)	#1	133.4	134.0	Not Available
400 F *	#1	364.3	366.0	347.5
	#2	362.6	364.3	345.0
	#3	369.4	371.3	351.3
	#4	367.6	369.6	350.9
60 F *	#1	57.6	58.1	53.3
	#2	59.6	60.1	54.4
	#3	59.6	60.1	54.4
	#4	57.5	58.0	54.1
25 F *	#1	24.5	24.6	22.3
	#2	24.1	24.3	22.0
	#3	24.5	24.6	22.3
10 F *	#1	9.82	9.88	9.01
	#2	9.63	9.68	8.90
	#3	9.88	9.94	9.05
	#4	9.58	9.62	8.92
1 F	#1	1.03	1.03	0.985
	#2	1.08	1.08	1.028
	#3	1.08	1.08	1.034
	#4	1.07	1.08	1.025

* The evaluation of capacitance using the CV technique presented in the table is the one performed with the lower scan rate (50 mV/s for 1 F, 50 mV/s for 10 F, 30 mV/s for 25 F, 10 mV/s for 60 F, and 5 mV/s for 400 F).

It is noted that the capacitance measured with cyclic voltammetry is significantly lower than that provided by the other two methods. To obtain higher capacitances, it would be necessary to use much lower scan rates, resulting in very long measurement times. This technique is not covered by the standards as a testing technique. Here, the analysis was primarily aimed at testing the model's ability to reproduce this type of test. For this purpose, the cycles were also simulated with the three-branch ECM. This latter is a current-driven model. Therefore, the measured current was used as the input to simulate the voltammetric cycles, and the cycles were reconstructed with the calculated voltages.

Even in the simulation, some cycles are necessary for stabilization, and the final cycles require a translation up to the origin. In some cases, the measured and calculated cycles are immediately superimposed; in other cases, the calculated cycles slightly exceed the nominal voltage by a maximum of 2–3%, and it is advisable to rescale them by a factor of 1.02–1.03 at most. This factor does not significantly affect the calculated capacitance. In fact, in agreement with (34), the area is slightly larger, but so is ΔV, and the ratio remains almost unchanged.

Figure 12 shows a comparison between the measured and simulated cycles, and the good overlap between the two is evident, in some cases almost perfect. Table 5 provides a more detailed comparison between the measured and calculated cycles. The table shows

the scaling factor. As can be seen, in most cases, the factor is 1, so the cycles naturally overlap, while rescaling was necessary, in other cases, but no more than 3%. Regarding capacitance, Table 6 shows the measured and computed capacitances and the percentage relative difference related to the measured one. The latter, in most cases, is less than 1%; in one case, it is 1.07%, and only in one case, it is 3.17%. Therefore, it is possible to state that the accuracy of the model in calculating the voltammetric cycles and the related capacitances is in line with the accuracy highlighted in the model identification reported in Section 4.2.

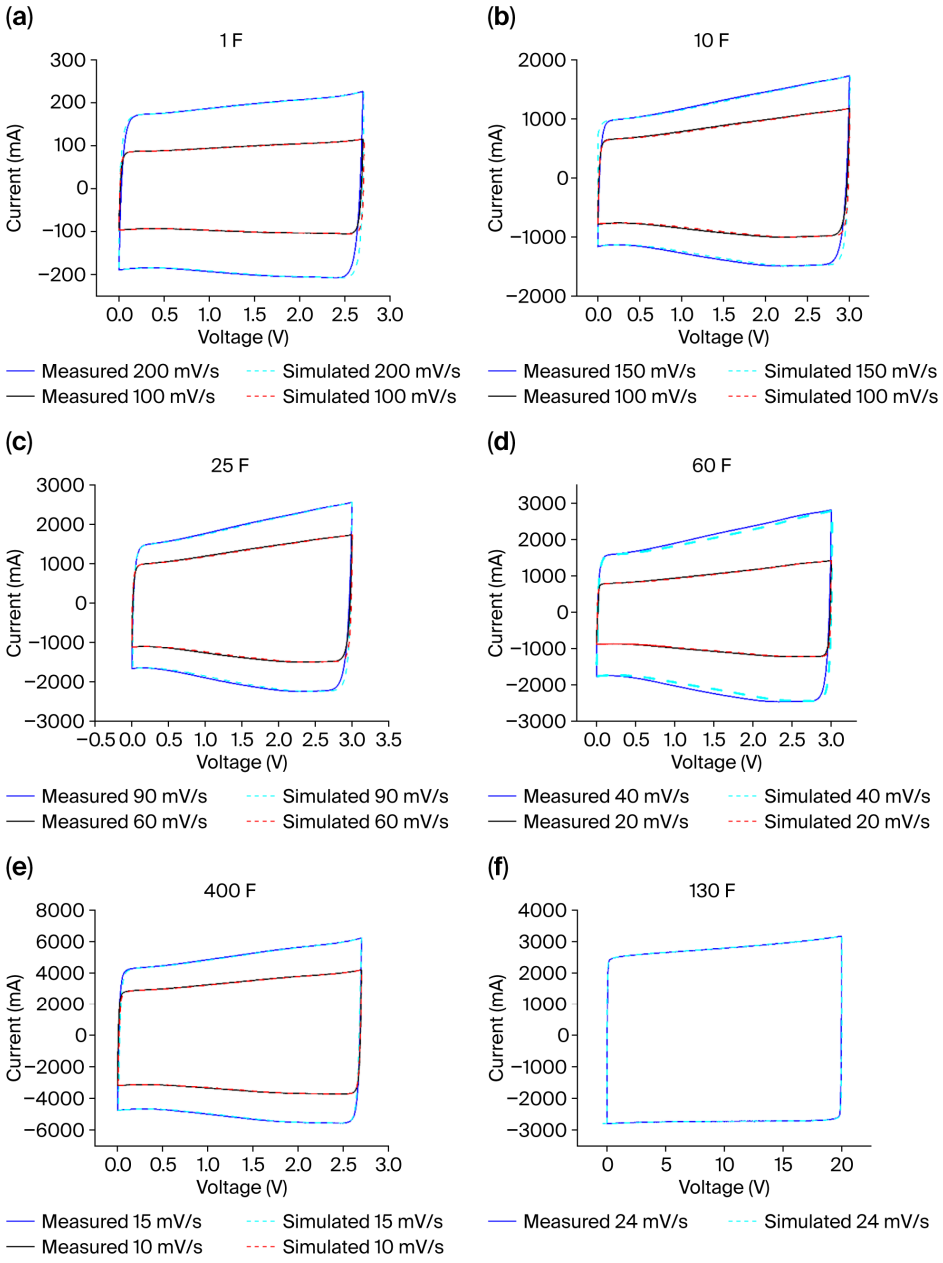

Figure 12. Measured and simulated CV curves for two different scan rates for the different SC sizes: (**a**) 1 F, scan rates 100 mV/s and 200 mV/s; (**b**) 10 F, scan rates 100 mV/s and 150 mV/s; (**c**) 25 F, scan rates 60 mV/s and 90 mV/s; (**d**) 60 F, scan rates 20 mV/s and 40 mV/s and (**e**) 400 F, scan rates 10 mV/s and 15 mV/s SCs. For the 130 F module (**f**), a single CV cycle was also measured at the scan rates of 24 mV/s, but only for model validation because the instrumentation was not able to reach the rated voltage of the device.

Table 6. Comparison between calculated and measured voltammetric cycles. The table shows the scaling factor (overlapping index between the measured and simulated cycle shape), the computed and measured capacitances, and the percentage relative difference between the calculated and measured capacitance, relayed to the measured one, in absolute value.

SC Size	Scaling Factor (to Overlap Graphically)	Scan Rate (mV/s)	Measured Capacitance (F)	Computed Capacitance (F)	Capacitance % Relative Difference
1 F	1.00	200	0.955	0.963	0.84
	1.00	100	0.980	0.978	0.20
10 F	1.08	150	8.652	8.700	0.55
	1.02	100	8.805	8.759	0.52
25 F	1.03	90	21.55	21.49	0.28
	1.02	60	21.89	21.87	0.09
60 F	1.00	40	52.93	51.25	3.17
	1.00	20	52.65	52.70	0.09
400 F	1.02	15	337.5	333.9	1.07
	1.01	10	340.9	339.6	0.38
130 F *	1.03	24	114.6 *	114.9	0.26

* The 130 F module capacitance is not significant. The voltammetric cycle was only run up to 20 V due to instrumentation limits. It is shown here only for comparison with the three-branch ECM.

Experimental CV cycles of EDLCs in Figure 12 show tilted or delayed shapes even in the absence of redox reactions. This behavior arises because real EDLCs are not ideal capacitors and exhibit internal resistance. Porous carbon electrodes lead to a distribution of relaxation times due to ion transport in pores of different sizes. As a result, electric double-layer charging is not instantaneous. Ion diffusion limitations further distort the ideal rectangular CV shape, especially at high scan rates. These effects may resemble slow redox kinetics but remain purely capacitive. A three-branch equivalent circuit can successfully reproduce the tilted and delayed CV response. The values of the voltage-dependent capacitance and *ESR* are intrinsically linked to the porosity and pore distribution on the electrode surface. So, the model captures the distributed capacitive and resistive behavior of EDLC electrodes [62].

5. Validation of Dynamic Behavior

Evaluating the dynamic behavior by applying a pulse train to the SC requires the use of a generator compliant with the generation of a clean signal. We tested several current-controlled voltage generators that showed conspicuous distortion limitations in generating the current signal; finally, we successfully tested the use of a transconductance current generator, the Clarke Hess model 8100 (Clarke-Hess Communications Research Corp, Medford, NY, USA) with a 40 ppm short-term stability, 0.04% accuracy in DC, and 0.10% accuracy in AC.

The signal for the transconductance amplifier was generated with a signal generator GW-Instek AFG-2012 (Good Will Instrument Co., New Taipei City, Taiwan), while the voltage and current were acquired using two synchronized Fluke 8588 A multimeters (Fluke Corporation, Everett, WA, USA), whose basic accuracy is better than 200 ppm for AC voltages up to 10 V and better than 1000 ppm for AC currents up to 10 A. The connections to SCs were formed with the four-terminal principle, like in all the other measurements. For the SCs cc and cv charging and discharging, we used Biologic BCS 810 or 815 modules and then inserted a switch to perform dynamic measurements with the system described above. A scheme of the generation and measurement system is shown in Figure 13.

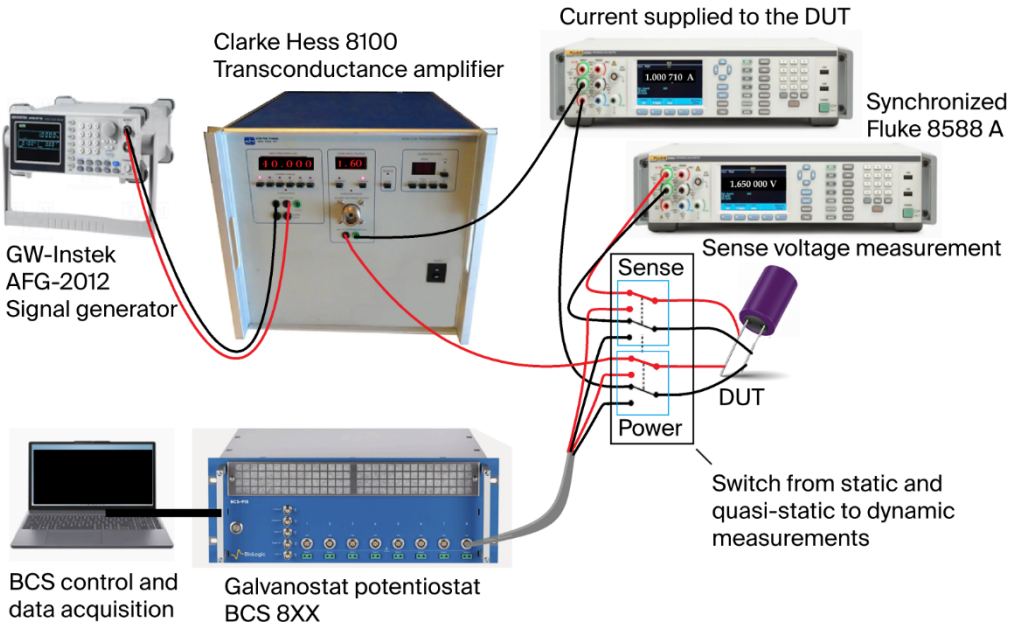

Figure 13. Scheme of the generation and measurement to combine static and dynamic tests.

The dynamic behavior was evaluated on a subset of the previously analyzed SCs, specifically 25 F, 60 F and 400 F. Current pulse trains at various frequencies were applied on each SC. The pulse's amplitude was held constant for all the measurements at about ±1 A. The examined frequency range spanned from 0.1 Hz and 100 Hz, including 1 Hz, 10 Hz, and 40 Hz. The sampling time chosen for the measurement was 500 µs for the frequencies 0.1 Hz, 1 Hz, and 10 Hz, while it was 50 µs for the higher frequencies 40 Hz and 100 Hz.

Each SC underwent a charge and self-discharge process to verify whether it matched the three-branch ECM identification. This is because, for some SCs, dynamic measurements were performed a few weeks after identification.

After this verification and subjecting the SC to further charging, if necessary, the equivalent circuit parameters shown in Table 4 were used. The measurements required preliminary charging of the SCs. This is because, otherwise, during dynamic measurements, an important and misleading voltage drift would be observed, which is limited if a stable terminal voltage is achieved after a recovery phase [63]; we call the stable voltage V_{start} in the following. For this purpose, the SCs were charged to the nominal voltage with cc charging, then subjected to 10 min of cv charging, and then discharged to a voltage close to the half of the rated voltage to perform the dynamic tests. An example is shown in Figure 14.

The circuit was simulated as follows. With the LTspice™ software, the ECM of the SC was replicated with the corresponding parameters (Figure 15). Two generators V_1 and V_2 are added to the circuit. Generator V_1 provides the SC with the starting test voltage terminal V_{start}, as recorded by the measurements. Generator V_2 controls the switch S_1 and is set as follows: $V_{init} = -1$ V, $V_{on} = 1$ V, $T_{on} = T_{start} - T_{period}/2$, where T_{period} is the period of the pulses, that is, the inverse of the frequency $T_{period} = 1/f$.

The current pulse train is generated by two current sources, I_1 and I_2; one provides positive pulses, while the other one provides the negative pulses. The parameters of the two generators are: I_{low}, I_{high}, T_{delay}, T_{rise}, T_{fall}, T_{on}, and T_{period}. I_{low} is zero; I_{high} is the measured pulse current (about −1 A for I_1 and about +1 A for I_2); T_{rise} and T_{fall} can be obtained from the measurements taking into account that, for higher frequencies (≥40 Hz), they can be different; T_{period} is $1/f$, while T_{on} is half of the period at the specific frequency; and T_{delay} is T_{start} for I_1 and $T_{start} + T_{on}$ for I_2.

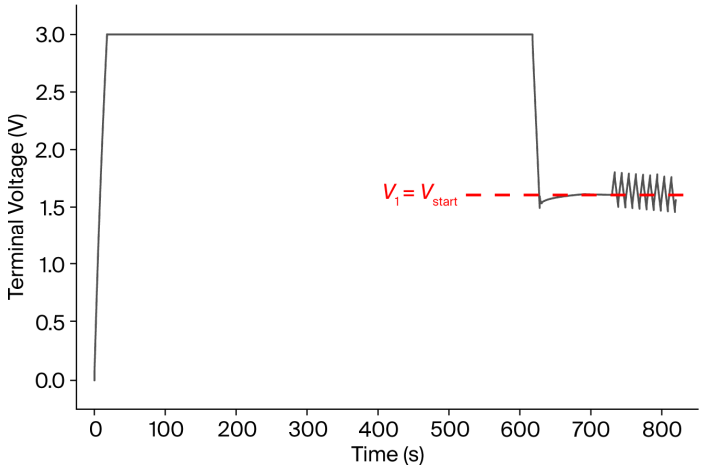

Figure 14. Example of a complete measurement cycle of the dynamic measurement test: cc plus cv, followed by a discharge to the test voltage; then, the dynamic excitation here is at 0.1 Hz. A sufficiently constant terminal voltage V_{start} is reached, which makes the voltage drift during dynamic tests negligible. At 0.1 Hz, the drift is still present but nearly negligible in the first periods and becomes even less significant at higher frequencies.

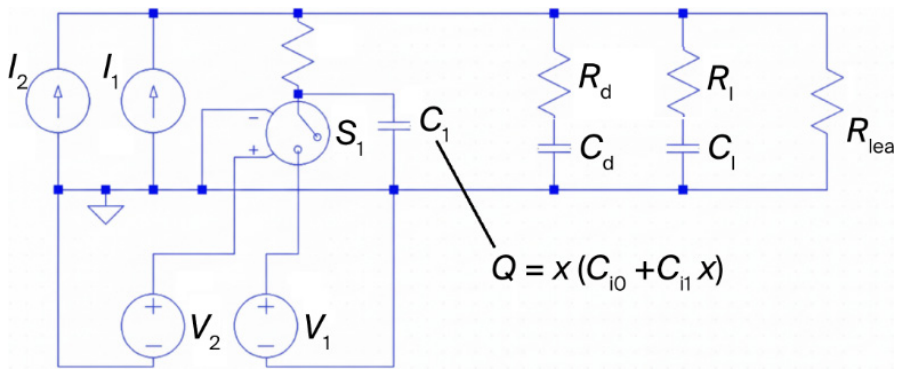

Figure 15. LTSpice^{TM} circuit for the generation of train pulses linked to the ECM of the SC.

Measurements and simulations are shown in Figure 16. The results highlight the following. As the frequency increases, small spikes appear in the measured voltage, close to the transition peaks. At 0.1 Hz, the simulation is very close to the measurements, with discrepancies on the order of 17 mV, over a peak-to-peak amplitude of 335 mV, which corresponds to a relative error of 5% or 0.62% if referring to the entire voltage range on which the simulation was based, which is the rated voltage of the SC as shown in Figure 14. The peak-to-peak amplitude of the voltage signal measured at the terminals, neglecting some small spikes that sometimes appear, decreases with frequency for the same current excitation. For the 25 F SC, the voltage peak-to-peak is from 335 mV at 0.1 Hz to 68 mV at 1 Hz, 42 mV at 10 Hz, 32 mV at 40 Hz, and 29 mV at 100 Hz. Furthermore, it decreases with the capacitance of the SCs. At 0.1 Hz, the peak-to-peak voltage goes from 335 mV for the 25 F SC to 133 mV for the 60 F SC and to 26 mV for the 400 F SC. At 100 Hz, the peak-to-peak terminal voltage is 29 mV for the 25 F SC, 16 mV for the 60 F SC, and 7 mV for the 400 F SC. The reduction in the voltage signal denotes an increase in the impedance at the frequency increase in this range and, as expected, also at the capacitance increase.

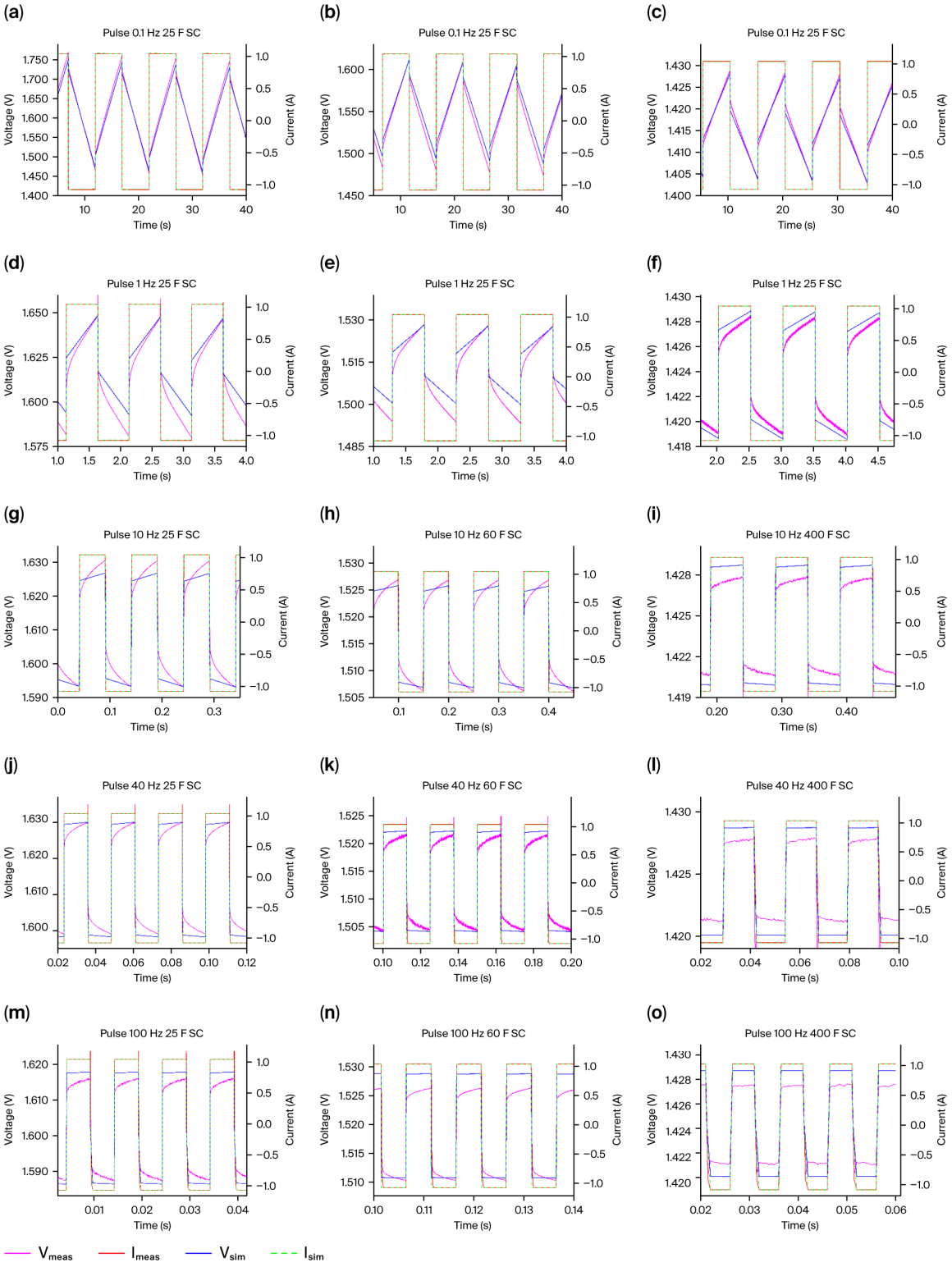

Figure 16. Terminal voltage response to the application of a train of current pulses with a peak amplitude of 1 A to the SCs. Three SCs were considered, with capacitances of 25 F, 60 F and 100 F. The terminal voltage values and flowing currents are represented with different colors: the measured voltage values are in magenta, and the calculated voltage values are in blue, while the imposed and measured current values are in red, and the simulated ones are in green. Each row contains the comparison for a specific frequency. First row, subfigures (**a**–**c**), 0.1 Hz. Second row, subfigures (**d**–**f**), 1 Hz. Third row, subfigures (**g**–**i**), 10 Hz. Fourth row, subfigures (**j**–**l**), 40 Hz. Fifth and last row, subfigures (**m**–**o**), 100 Hz.

Some specific observations can be made.

- At 0.1 Hz and 1 Hz, the effect of capacitance is greater, while at higher frequencies, resistance plays a more significant role than capacitance. The capacitive effect changes over time after the transition and then, after a certain period, follows the behavior predicted by the model. Considering the derivative of the voltage as a function of time after each transition, one can calculate the differential capacitance, which is small immediately after the transition and approaches the model capacitance (the slope of the simulated curve) after fractions of a second. Assuming exponential behavior, the time constant is around 0.2 s.
- The 1 Hz curves can provide the best information on the settling time constant, even though at higher frequencies, something similar should happen, but the transition does not occur completely in the half-period, and the slope of the voltage curve at constant current does not approach the slope given by the simulation.
- In the curves with frequencies above 10 Hz, especially for the 25 F and 60 F capacitors, a reduction in resistance is also noted (a smaller jump at the transition step), probably due to the incomplete achievement of equilibrium in the distribution of the electrical charges.
- For the 400 F SC, the dynamic resistance is always lower than that obtained by optimizing the parameters, even though the difference becomes more pronounced for frequencies above 10 Hz.

Beyond the discussion of discrepancies between computed and measured values and their causes, it should be noted that the differences are always limited. For example, at 1 Hz and 10 Hz, we can consider the 25 F SC, while at 40 Hz and 100 Hz, we consider the 400 F SC: in these two cases, the largest discrepancies can be noticed. In the first case, at 1 Hz, the measured peak-to-peak voltage is 68 mV against the computed 56 mV, with a difference of 12 mV, equal to 0.4% of the rated voltage. At 10 Hz, against a measured peak-to-peak voltage of 42 mV, the computed one is 34 mV, with a difference equal to 8 mV or 0.27% of the rated voltage. For the 400 F SC at 40 Hz, the measured peak-to-peak voltage is 17 mV, while the calculated one is 9 mV, again with a difference of 8 mV or 0.27% of the rated voltage. At 100 Hz, the measured peak-to-peak voltage is 7 mV, while the computed one is 8.7 mV or less than 0.1% of the rated voltage.

The three-branch model is identified in static conditions with an accuracy better than 3% of the rated voltage. Under dynamic conditions, its behavior is quite good, providing a prediction of the dynamic response better than 1% of the rated voltage.

It should be noted that the identification was performed across the entire rated voltage range, optimizing the parameters during a full charge and long self-discharge phase. For specific dynamic applications, with response times of milliseconds or tens of milliseconds and limited voltage response span, it is possible to consider a specific and targeted identification to further optimize the model's response, which, nevertheless, remains that of a good design and control tool in electrical engineering applications.

6. Discussion and Conclusions

The results shown in this paper demonstrate a strong correspondence between the model simulations and the experimental measurements for response in the time span from milliseconds to hours, charging currents from 500 mA to 440.5 A, and rated voltages from 2.7 V to 62 V. This agreement is particularly relevant from an electrotechnical standpoint because it directly affects the accurate determination of the terminal voltage as it is influenced by the device's prior charging history because different time constants are involved in the response of the device. The identification of the ECM thus enables more effective control of the SC, whose behavior can be reliably predicted by the model.

This extensive validation of the three-branch model allows it to be proposed for consideration as a standard. From it, the main parameters of an SC, such as stored energy and maximum power, can be deduced. It also provides a tool for evaluating its voltammetric cycles and its static and dynamic responses in energy applications, with an accuracy certainly much better than 5%.

The dynamic analysis of the three-branch model presented here effectively addresses the need for accurate time-response predictions for fast pulses in modern SC applications. The model validated in this study is a reliable design tool that, differently from EIS analysis, provides the time-response to a fast pulse excitation. The results presented here can be further improved by performing identification tuning aimed at the voltage range and actuation frequency required by specific applications.

Author Contributions: Conceptualization, M.Z.; methodology, M.Z., M.H., O.C. and U.P.; software, M.Z., M.H. and O.C.; validation, M.Z., M.H., O.C. and U.P.; formal analysis, M.Z. and U.P.; investigation, M.Z., M.H., O.C. and U.P.; resources, M.Z.; data curation, M.H. and O.C.; writing—original draft preparation, M.Z., M.H., O.C. and U.P.; writing—review and editing, M.H., O.C., U.P. and V.G.; supervision, project administration, and funding acquisition, M.Z.; assembly, mounting operations and validation of test systems, V.G. All authors have read and agreed to the published version of the manuscript.

Funding: This study has been developed in the framework of the 23IND04 MetSuperCap Project, which has received funding from the European Partnership on Metrology, co-financed by the European Union's Horizon Europe Research and Innovation Programme and by the Participating States. The views and opinions expressed are, however, those of the authors only and do not necessarily reflect those of the European Union or EURAMET. Neither the European Union nor the granting authority can be held responsible for them.

Data Availability Statement: Most of the data produced in this research can be downloaded in detail, with the datasets published in the public database Zenodo, at the addresses reported in the references from [41–60].

Acknowledgments: The authors are grateful to Davide Signorino for the assistance and advice provided during the measurements. The authors used AI (Gemini™ specifically 3.1 Pro) to improve the quality of some figures and of some sentences.

Conflicts of Interest: The authors declare no conflicts of interest.

Abbreviations

The following abbreviations are used in this manuscript:

cc	Constant-Current
ch-dis	Charge–Discharge
ch-sd	Charge–Self discharge
CPE	Constant Phase Element
CTRR	Conventional Trust Region Reflection Method
CV	Cyclic Voltammetry
cv	Constant-Voltage
ECM	Equivalent Circuit Model
EDLC	Electric Double-Layer Capacitor
EIS	Electrical Impedance Spectroscopy
ESR	Equivalent Series Resistance
FO	Fractional Order Model
FOEC	Fractional-Order Equivalent Circuit
GCD	Galvanostatic Charge–Discharge

GCSD	Galvanostatic Charge–Self-discharge
HESS	Hybrid Energy Storage Systems
SC	Supercapacitor
SoH	State of Health
TLM	Transmission Line Model
UPS	Uninterruptible Power Supply

References

1. Zhao, J.; Burke, A.F. Review on supercapacitors: Technologies and performance evaluation. *J. Energy Chem.* **2021**, *59*, 276–291. [CrossRef]
2. Oyedotun, K.O.; Mamba, B.B. New trends in supercapacitors applications. *Inorg. Chem. Commun.* **2024**, *170*, 113154. [CrossRef]
3. Automobili Lamborghini S.p.A. Lamborghini Sian FKP 37. 2025. Available online: https://www.lamborghini.com/en-en/models/limited-series/sian-fkp-37 (accessed on 10 January 2026).
4. Wang, B.; Wang, C.; Wang, Z.; Ni, S.; Yang, Y.; Tian, P. Adaptive State of Energy Evaluation for Supercapacitor in Emergency Power System of More-Electric Aircraft. *Energy* **2023**, *263*, 125632. [CrossRef]
5. Xie, X.; Shen, W.; Chen, H.; Gao, N.; Yang, Y.; Saim, A.; Benbouzid, M. Optimization Strategies for Hybrid Energy Storage Systems in Fuel Cell-Powered Vessels Using Improved Droop Control and POA-Based Capacity Configuration. *J. Mar. Sci. Eng.* **2026**, *14*, 58. [CrossRef]
6. Corti, F.; Laudani, A.; Lozito, G.M.; Palermo, M.; Quercio, M.; Pattini, F.; Rampino, S. Dynamic Analysis of a Supercapacitor DC-Link in Photovoltaic Conversion Applications. *Energies* **2023**, *16*, 5864. [CrossRef]
7. Naseri, F.; Karimi, S.; Farjah, E.; Schaltz, E. Supercapacitor management system: A comprehensive review of modeling, estimation, balancing, and protection techniques. *Renew. Sustain. Energy Rev.* **2022**, *155*, 111913. [CrossRef]
8. Chaudhari, S.A.; Patil, V.V.; Jadhav, V.A.; Thorat, P.; Sutar, S.S.; Dongale, T.D.; Parale, V.; Patil, V.; Mhamane, D.S.; Mali, M.G.; et al. Conductivity boosted BiVO4 for enhanced OER and supercapacitive performance: Stability insights with modeling, predictions, and forecasting using machine learning technique. *Energy Mater.* **2025**, *5*, 500082. [CrossRef]
9. Navarro, G.; Torres, J.; Blanco, M.; Nájera, J.; Santos-Herran, M.; Lafoz, M. Present and Future of Supercapacitor Technology Applied to Powertrains, Renewable Generation and Grid Connection Applications. *Energies* **2021**, *14*, 3060. [CrossRef]
10. Jami, M.; Shafiee, Q.; Gholami, M.; Bevrani, H. Control of a super-capacitor energy storage system to mimic inertia and transient response improvement of a direct current micro-grid. *J. Energy Storage* **2020**, *32*, 101788. [CrossRef]
11. Dissanayake, K.; Kularatna-Abeywardana, D. A review of supercapacitors: Materials, technology, challenges, and renewable energy applications. *J. Energy Storage* **2024**, *96*, 112563. [CrossRef]
12. Sayed, I.A.; Mahmoud, Y. Robust hybrid Neural–Kalman filter for real-time supercapacitor state-of-charge estimation in electric vehicles. *Future Batter.* **2025**, *8*, 100115. [CrossRef]
13. Şahİn, M.E.; Blaabjerg, F.; SangwongwanİCh, A. Modelling of supercapacitors based on simplified equivalent circuit. *CPSS Trans. Power Electron. Appl.* **2021**, *6*, 31–39. [CrossRef]
14. Slaifstein, D.; Ibanez, F.M.; Siwek, K. Supercapacitor Modeling: A System Identification Approach. *IEEE Trans. Energy Convers.* **2023**, *38*, 192–202. [CrossRef]
15. Morandi, A.; Lampasi, A.; Cocchi, A.; Gherdovich, F.; Melaccio, U.; Ribani, P.L.; Rossi, C.; Soavi, F. Characterization and Model Parameters of Large Commercial Supercapacitor Cells. *IEEE Access* **2021**, *9*, 20376–20390. [CrossRef]
16. Castiglia, V.; Campagna, N.; Di Tommaso, A.O.; Miceli, R.; Nevoloso, C.; Pellitteri, F.; Puccio, C.; Viola, F. Modeling, Simulation, and Characterization of a Supercapacitor in Automotive Applications. *IEEE Trans. Ind. Appl.* **2022**, *58*, 2421–2429. [CrossRef]
17. Marín-Coca, S.; Ostadrahimi, A.; Bifaretti, S.; Roibás-Millán, E.; Pindado, S. New Parameter Identification Method for Supercapacitor Model. *IEEE Access* **2023**, *11*, 21771–21782. [CrossRef]
18. Lemian, D.; Bode, F.I.; Lapusan, C. Enhancing Supercapacitor Simulation Accuracy Through a Novel Hybrid Modeling Approach. *Appl. Sci.* **2025**, *15*, 226. [CrossRef]
19. Shaheen, M.A.; Hasanien, H.M.; Ullah, Z.; Alferidi, A.; Alsolami, M.; Lami, B. Hybrid osprey-parrot optimization algorithm for enhanced parameter identification of supercapacitor model. *J. Energy Storage* **2025**, *137*, 118604. [CrossRef]
20. De Carne, G.; Morandi, A.; Karrari, S. Supercapacitor Modeling for Real-Time Simulation Applications. *IEEE J. Emerg. Sel. Top. Ind. Electron.* **2022**, *3*, 509–518. [CrossRef]
21. Rasoolzadeh, A.; Hashemi, S.A.; Pahlevani, M. Online Identification of Differential Order in Supercapacitor Fractional-Order Models: Advancing Practical Implementation. *Energies* **2025**, *18*, 1876. [CrossRef]
22. Maity, S.; Saha, M.; Saha, P.; Khanra, M. Fractional calculus-based modeling and state-of-charge estimation of supercapacitor. *J. Energy Storage* **2024**, *81*, 110317. [CrossRef]

23. Zhang, Q.; Wei, K. A comparative study of fractional-order models for supercapacitors in electric vehicles. *Int. J. Electrochem. Sci.* **2024**, *19*, 100441. [CrossRef]
24. Ottoboni, K.A.; da Cruz, P.V.D.; Faria, R.N. Optimized fractional order resonant model of supercapacitors based in error dominant frequency mitigation. *Future Batter.* **2024**, *4*, 100012. [CrossRef]
25. Hardianto, Y.P.; Shah, S.S.; Shuaibu, A.D.; Mohamed, M.; Sarker, S.; Alzahrani, A.S.; Aziz, A. Modeling supercapacitors with the simplified Randles circuit: Analyzing electrochemical behavior through cyclic voltammetry and Galvanostatic charge-discharge. *Electrochim. Acta* **2025**, *513*, 145552. [CrossRef]
26. Rus-Casas, C.; Ramos-Paja, C.A.; Serna-Garcés, S.I.; Gilabert-Torres, C.; Aguilar-Peña, J.D. A Circuital Equivalent for Supercapacitors Accurate Simulation in Power Electronics Systems. *Batteries* **2025**, *11*, 307. [CrossRef]
27. Zubieta, L.; Bonert, R. Characterization of double-layer capacitors for power electronics applications. *IEEE Trans. Ind. Appl.* **2000**, *36*, 199–205. [CrossRef]
28. Prasad, R.; Mehta, U.; Kothari, K.; Cirrincione, M.; Mohammadi, A. Supercapacitor Parameter Identification Using Grey Wolf Optimization and Its Comparison to Conventional Trust Region Reflection Optimization. In Proceedings of the 2019 International Aegean Conference on Electrical Machines and Power Electronics (ACEMP) & 2019 International Conference on Optimization of Electrical and Electronic Equipment (OPTIM), Istanbul, Turkey, 27–29 August 2019; pp. 563–569. [CrossRef]
29. Zucca, M.; Hassanzadeh, M.; Conti, O.; Pogliano, U. Accurate Parameters Identification of a Supercapacitor Three-Branch Model. *IEEE Access* **2023**, *11*, 122387–122398. [CrossRef]
30. Zucca, M.; Hassanzadeh, M.; Signorino, D.; Pogliano, U. Uncertainty Evaluation of a Supercapacitor Equivalent Circuit Parameters. *IEEE Trans. Instrum. Meas.* **2025**, *74*, 1502509. [CrossRef]
31. Ivanov, V.D. The Helmholtz model. *J. Solid State Electrochem.* **2024**, *28*, 2487–2493. [CrossRef]
32. *EN 62391-2:2006*; Fixed Electric Double-Layer Capacitors for Use in Electronic Equipment—Part 2: Sectional Specification—Electric Double Layer Capacitors for Power Application. CEN-CENELEC: Brussels, Belgium, 2006; the last update is IEC 62391-2:2025.
33. *EN IEC 62576:2018*; Electric Double-Layer Capacitors for Use in Hybrid Electric Vehicles—Test Methods for Electrical Characteristics. CEN-CENELEC: Brussels, Belgium, 2018.
34. De Levie, R. On porous electrodes in electrolyte solutions. *Electrochim. Acta* **1963**, *8*, 751–780. [CrossRef]
35. Garcia-Belmonte, G.; Fabregat-Santiago, F.; Bisquert, J.; Yamashita, M.; Pereira, E.C.; Castro-Garcia, S. Frequency dispersion in electrochromic devices and conducting polymer electrodes: A generalized transmission line approach. *Ionics* **1999**, *5*, 44–51. [CrossRef]
36. Landesfeind, J.; Hattendorff, J.; Ehrl, A.; Wall, W.A.; Gasteiger, H.A. Tortuosity Determination of Battery Electrodes and Separators by Impedance Spectroscopy. *J. Electrochem. Soc.* **2016**, *163*, A1373. [CrossRef]
37. Rasoolzadeh, A.; Hashemi, S.A.; Pahlevani, M. A Fractional-Order State Estimation Method for Supercapacitor Energy Storage. *Electronics* **2025**, *14*, 3231. [CrossRef]
38. Yasin, A.; Dhaouadi, R.; Mukhopadhyay, S. A Novel Supercapacitor Model Parameters Identification Method Using Metaheuristic Gradient-Based Optimization Algorithms. *Energies* **2024**, *17*, 1500. [CrossRef]
39. Campagna, N.; Castiglia, V.; Gennaro, F.; Messina, A.A.; Miceli, R. Fuel Cell-Based Inductive Power Transfer System for Supercapacitor Constant Current Charging. *Energies* **2024**, *17*, 3575. [CrossRef]
40. Zucca, M.; Al-Zubaidi-R-Smith, N.; Bartova, L.; Brom, H.v.D.; Callegaro, L.; Cultrera, A.; Fast, L.; Girimonte, A.; Hassanzadeh, M.; Mariscotti, A.; et al. MetSuperCap: Metrology for static and dynamic characterisation of supercapacitors. *Meas. Sens.* **2025**, *38*, 101434. [CrossRef]
41. Zucca, M.; Hassanzadeh, M.; Pogliano, U.; Conti, O.; Valter, G. INRIM_Brand1_1F_1_23C_0k_EDLC_single (1.0). [Data Set]. Zenodo 2026. Available online: https://zenodo.org/records/18348131 (accessed on 28 January 2026).
42. Zucca, M.; Hassanzadeh, M.; Pogliano, U.; Conti, O.; Giusio, V. INRIM_Brand1_1F_2_23C_0k_EDLC_single (1.0). [Data Set]. Zenodo 2026. Available online: https://zenodo.org/records/18348268 (accessed on 28 January 2026).
43. Zucca, M.; Hassanzadeh, M.; Conti, O.; Pogliano, U.; Giusio, V. INRIM_Brand1_1F_3_23C_0k_EDLC_single (1.0). [Data Set]. Zenodo 2026. Available online: https://zenodo.org/records/18348738 (accessed on 28 January 2026).
44. Zucca, M.; Hassanzadeh, M.; Conti, O.; Pogliano, U.; Giusio, V. INRIM_Brand1_1F_4_23C_0k_EDLC_single (1.0). [Data Set]. Zenodo 2026. Available online: https://zenodo.org/records/18350649 (accessed on 28 January 2026).
45. Zucca, M.; Hassanzadeh, M.; Pogliano, U.; Conti, O.; Giusio, V. INRIM_Brand1_10F_1_23C_0k_EDLC_single (1.0). [Data Set]. Zenodo 2025. Available online: https://zenodo.org/records/17763055 (accessed on 28 January 2026).
46. Zucca, M.; Hassanzadeh, M.; Pogliano, U.; Conti, O.; Giusio, V. INRIM_Brand1_10F_2_23C_0k_EDLC_single (1.0). [Data Set]. Zenodo 2025. Available online: https://zenodo.org/records/17763259 (accessed on 28 January 2026).
47. Zucca, M.; Hassanzadeh, M.; Pogliano, U.; Conti, O.; Giusio, V. INRIM_Brand1_10F_3_23C_0k_EDLC_single (1.0). [Data Set]. Zenodo 2025. Available online: https://zenodo.org/records/17763477 (accessed on 28 January 2026).

48. Zucca, M.; Hassanzadeh, M.; Pogliano, U.; Conti, O.; Giusio, V. INRIM_Brand1_10F_4_23C_0k_EDLC_single (1.0). [Data Set]. Zenodo 2026. Available online: https://zenodo.org/records/18351123 (accessed on 28 January 2026).
49. Zucca, M.; Hassanzadeh, M.; Pogliano, U.; Giusio, V.; Conti, O. INRIM_Brand1_25F_1_23C_0k_EDLC_single (1.0). [Data Set]. Zenodo 2025. Available online: https://zenodo.org/records/17762767 (accessed on 28 January 2026).
50. Zucca, M.; Hassanzadeh, M.; Pogliano, U.; Conti, O.; Giusio, V. INRIM_Brand1_25F_2_23C_0k_EDLC_single (1.0). [Data Set]. Zenodo 2025. Available online: https://zenodo.org/records/17762845 (accessed on 28 January 2026).
51. Zucca, M.; Hassanzadeh, M.; Pogliano, U.; Conti, O.; Giusio, V. INRIM_Brand1_25F_3_23C_0k_EDLC_single (1.0). [Data Set]. Zenodo 2025. Available online: https://zenodo.org/records/17762913 (accessed on 28 January 2026).
52. Zucca, M.; Hassanzadeh, M.; Pogliano, U.; Conti, O.; Giusio, V. INRIM_Brand1_60F_1_23C_0k_EDLC_single (1.0). [Data Set]. Zenodo 2025. Available online: https://zenodo.org/records/17761575 (accessed on 28 January 2026).
53. Zucca, M.; Hassanzadeh, M.; Pogliano, U.; Conti, O.; Giusio, V. INRIM_Brand1_60F_2_23C_0k_EDLC_single (1.0). [Data Set]. Zenodo 2025. Available online: https://zenodo.org/records/17761703 (accessed on 28 January 2026).
54. Zucca, M.; Hassanzadeh, M.; Pogliano, U.; Conti, O.; Giusio, V. INRIM_Brand1_60F_3_23C_0k_EDLC_single (1.0). [Data Set]. Zenodo 2025. Available online: https://zenodo.org/records/17761788 (accessed on 28 January 2026).
55. Zucca, M.; Hassanzadeh, M.; Conti, O.; Conti, O.; Giusio, V. INRIM_Brand1_60F_4_23C_0k_EDLC_single (1.0). [Data Set]. Zenodo 2026. Available online: https://zenodo.org/records/18350909 (accessed on 28 January 2026).
56. Zucca, M.; Hassanzadeh, M.; Pogliano, U.; Conti, O.; Giusio, V. INRIM_Brand1_400F_1_23C_0k_EDLC_single (1.0). [Data Set]. Zenodo 2025. Available online: https://zenodo.org/records/17748936 (accessed on 28 January 2026).
57. Zucca, M.; Hassanzadeh, M.; Pogliano, U.; Giusio, V. INRIM_Brand1_400F_2_23C_0k_EDLC_single (1.0). [Data Set]. Zenodo 2025. Available online: https://zenodo.org/records/17761192 (accessed on 28 January 2026).
58. Zucca, M.; Hassanzadeh, M.; Conti, O.; Giusio, V.; Pogliano, U. INRIM_Brand1_400F_3_23C_0k_EDLC_single (1.0). [Data Set]. Zenodo 2025. Available online: https://zenodo.org/records/17761348 (accessed on 28 January 2026).
59. Zucca, M.; Hassanzadeh, M.; Conti, O.; Pogliano, U.; Giusio, V. INRIM_Brand1_400F_4_23C_0k_EDLC_single (1.0). [Data Set]. Zenodo 2025. Available online: https://zenodo.org/records/18351600 (accessed on 28 January 2026).
60. Zucca, M.; Hassanzadeh, M.; Pogliano, U.; Conti, O.; Giusio, V. INRIM_Brand1_130F_1_23C_0k_EDLC_Module (1.0). [Data Set]. Zenodo 2026. Available online: https://zenodo.org/records/18365953 (accessed on 28 January 2026).
61. Conway, B.E. *Electrochemical Supercapacitors: Scientific Fundamentals and Technological Applications*; Kluwer Academic/Plenum Publishers: New York, NY, USA, 1999.
62. Chatterjee, K.; Basu, S.; Gupta, N. Modelling of an electrochemical double layer capacitor using cyclic voltammetry. In Proceedings of the 2021 IEEE Electrical Insulation Conference (EIC), Denver, CO, USA, 7–28 June 2021; pp. 355–358. [CrossRef]
63. Liu, D.; Kirk, D.W.; Jia, C.Q. A physical model of a supercapacitor to reveal the mechanism of the voltage recovery phenomenon. *Chem. Commun.* **2023**, *59*, 8428–8431. [CrossRef]